ORIGINAL ARTICLE

Journal Section

Context-aware UAV LiDAR reveals forest structure and improves tree diameter estimates in subalpine forest

Jaime C. Revenga[1,2,3] | Stefan Oehmcke[4,5] | Mana Gharun[6] | Flurin Sutter[7] | Fabian Gieseke[5,8] | Katerina Trepekli[9] | Nina Buchmann[10] | Alexander Damm[11,12]

[1]Department of Biology, Section for Ecoinformatics and Biodiversity, Aarhus University, Denmark.

[2]Center for Landscape Research in Sustainable Agricultural Futures (Land-CRAFT), Aarhus University, Ole Worms Allé 3, 8000 Aarhus, Denmark

[3]Deparment of Geosciences and Natural Resources Management, University of Copenhagen, Øster Volgade 10, 1350 Copenhagen, Denmark.

[4]Institute for Visual and Analytic Computing, University of Rostock, Albert-Einstein-Straße 21, 18059 Rostock, Germany.

[5]Department of Computer Science, University of Copenhagen, Universitetsparken 1, 2100 Copenhagen, Denmark.

[6]Institute of Landscape Ecology, Research Unit for Biosphere-Atmosphere Interaction, University of Münster, Heisenbergstr. 2, 48149 Münster, Germany.

[7]Swiss Federal Institute for Forest, Snow and Landscape Research (WSL), Forest Dynamics Research Unit, Zürcherstrasse 111, 8903 Birmensdorf, Switzerland.

[8]Machine Learning and Data Engineering, Department of Information Systems, University of Münster, Leonardo Campus 3, 48149 Münster, Germany.

[9]Department of Geology and Geoenvironment, National and Kapodistrian University of Athens, University Campus 157 72, Zografou, Athens, Greece.

[10]Department of Environmental Systems

Forest structure, tree diameter, and aboveground biomass (AGB) are central variables in trait-based ecology and forest management, and recent advances in Unmanned Aerial Vehicle (UAV) and LiDAR surveys have substantially improved tree-level phenotyping of these structural attributes. Building on these developments, machine-learning (ML) applications are increasingly used to refine tree-diameter estimates and, by extension, improve AGB predictions derived from allometric relationships. Here, we evaluated the capacity of shallow learning methods to leverage local information from the surrounding context of the tree of interest to improve predictions of stem diameter and tree-level biomass, over 33 ha of a Norway spruce forest (Davos, CH). Our objectives were to (i) characterise gradients in tree height, (ii) examine group-level morphology of tree assemblages as an indicator of forest structural organisation, and (iii) assess whether these patterns can be leveraged to improve tree diameter and AGB predictions. We segmented the point cloud data scene into individual canopies and focused on LiDAR-derived tree canopy features. We then used local indicators of spatial association of tree heights to characterize local context and identified tree assemblages within the forest. Assemblage-level metrics were first analysed to characterise forest spatial structure and ecological similarity, and subsequently evaluated as additional predictors in ML regression experiments for tree diameter. The focus was on comparing performance of tree diameter predictions between twin regression methods that either consider assemblage metrics (i.e. context-aware), or not. Then, the improvements provided by context awareness were assessed in terms of accuracy gained in estimating tree diameter and AGB. We obtained results of three different shallow learning methods and evaluated these based on nested cross-validation. We considered two datasets within the same site: one being scattered in sparse measurement plots, the other spatially continuous. In both sparse and continuous datasets, we found enhanced prediction performance in context-aware regressions, where RMSE on tree diameter estimation was reduced by 4.1% and by 0.8%, respectively, suggesting that an heterogeneous context supports enhanced estimates. These findings indicate that gradients in tree height can reflect underlying ecological drivers of forest structure, and that this structural information may be leveraged to enhance predictions of tree diameter and AGB. The method proposed is fully native to UAV LiDAR data.

KEYWORDS
forest structure, tree diameter, aboveground biomass, environmental monitoring, machine learning, context-aware modeling, LiDAR, UAV

This manuscript is a preprint, and it is currently considered for publication. Code and data will be made available upon acceptance for publication.

1 | INTRODUCTION

Natural forests exhibit complex structures shaped by underlying ecological processes such as competition, facilitation, acclimation and disturbance dynamics. These processes influence tree structure and aboveground biomass (AGB), both of which are key variables in forest ecology and management. AGB plays a major role in determining global carbon budgets, and forests are essential for regulating carbon exchange between the atmosphere and the biosphere [1, 2]. Despite substantial advances in environmental remote sensing, current assessments of forest carbon cycling remain uncertain, with contrasting findings partly attributed to limited accuracy in AGB estimation [3, 4, 5]. This highlights the need for methods that improve characterization of forest spatial structure and improve accuracy and spatial resolution of forest AGB estimates from remotely sensed data [6].

Predictive analyses in forest phenotyping and AGB from remote sensing surveys have traditionally been focused on regressions considering only individual tree attributes as predictors (e.g. tree height, canopy metrics) [7, 8] and fitted allometric models [9]. Such tree-level analyses have been crucial for improving the characterization of optical vegetation traits [10], tree dendrometry [11], and species composition [12]. However, these approaches generally do not account for the influence of spatial context on the individual tree traits under investigation, including both abiotic factors (e.g., terrain conditions, soil depth) and biotic interactions (e.g., light interception, nutrient competition). Moreover, it is well established that local context—encompassing microclimatic, edaphic, and biotic conditions—strongly shapes tree traits, and that individual tree performance is influenced by the combined effects of abiotic stress and biotic interactions [13, 14]. Moreover, a line of research has aimed to measure tree performance components (e.g. stature, dominance, wood density) across environmental gradients, while monitoring local biotic interactions [15, 16]. Indeed, an increasing number of empirical studies, have proposed different methods to use the information of neighboring trees to enhance individual tree trait estimates (i.e. metrics derived from monitoring inventory plots), such as non-linear mixed effects methods [17, 18, 19], or competition-based methods [20, 21, 22]. This line of research has shown that considering neighborhood information can improve trait estimates, and its positive impact has been documented in various tree-level regression analyses, e.g. productivity [23, 24], fuel potential [25] or structural metrics [19, 26, 27].

However, despite the utility of current methods that leverage neighborhood metrics such as tree stand information, from an object-based remote sensing perspective they result suboptimal in some respects. Many of such methods are not directly transferable to a remote sensing framework because they use understory metrics as predictors (e.g. stem diameter of neighboring trees), which are difficult to survey reliably from an above-canopy perspective [20, 21]. Additionally, questions remain about the optimal scale at which such neighborhood metrics become relevant and therefore should be retrieved [23, 24]. A common procedure is to consider the trees contained in an arbitrarily delineated inventory plot, whose size is defined to fit management purposes [24]. This approach, although useful for monitoring tasks, can pose the shortcoming of overlooking the spatial scale at which relevant ecological phenomena operate (e.g. the appropriate range at which tree competition effects are significant), so the analysis remains constrained by the effects observed at the scale of the plot size [17, 18, 19, 20, 21]. To the best of our knowledge, tree-level AGB and trait assessments considering neighborhood information are currently limited due to one or more of the following reasons: (i) they characterize the spatial context with uniquely process-specific indices (e.g. competition pressure from immediate neighbors) [20, 21, 22]; (ii) they calibrate models with neighborhood-metrics retrieved from artificially-bounded inventory plots (e.g. nonlinear mixed-effects methods) [17, 18, 19]; or (iii) they overlook the spatial scale at which an ecological phenomenon affects the trait under investigation. Moreover, when the relationship between the plot-level predictors used and any ecological phenomenon is described, often ancillary data sources are incorporated (e.g. tree stand age) [21, 28] or less strictly quantified forest management metrics, e.g. "stand quality", "site index", "dominance index" [18, 21, 28]. These shortcomings are constrained by the specific data collection protocol, and currently hinder transferring such methods to an integrated remote sensing framework, which would offer greater flexibility for conducting standardized, scalable, and replicable forest analyses.

Unstaffed Aerial Vehicles (UAV) equipped with Light Detection and Ranging (LiDAR) monitoring systems are regarded as particularly versatile [29], accurate and cost-effective tools [30] to contribute to the task of extensive phenotyping, bridging scales in AGB mapping, particularly covering the scale between *in situ* field-based inventories (approx. 0-1 ha) and airborne LiDAR datasets (approx. 1-10^4 km^2) [31, 32]. With a surveying accuracy comparable to field-based measurements, UAV LiDAR monitoring provides datasets (i.e. point cloud data, PCD) that allow high throughput individual tree phenotyping at an intermediate spatial scale (approx. 1-40 ha).

While it is commonly argued that understanding local ecological processes in forests requires monitoring metrics (e.g. structure, biomass) of individual trees [21, 23, 24, 33], the reverse perspective is seldom discussed: how and to what extent can community ecology processes be harnessed in tree-level regression experiments? Earlier works have proposed to account for the effects of immediate competition pressure on tree growth with either distance-based [22] or distance-independent metrics [20, 34], generally finding such approaches beneficial to improve tree level estimates [20, 21]. However, these studies are based on the premise that competition indices are the determining factor conditioning tree development, while overlooking other potential regulation factors. In this scenario, nonparametric ML regression methods, which do not assume preexisting distributions or premises, are a sound approach to incorporate a contextual analysis, and have been proposed in previous forest mapping studies [35].

Context-based regression studies [36, 37] have shown in the last decade that the inclusion of information of local context (i.e. information about the surroundings of the target object) may improve model performance as a result of consistent spatial correlations [38]. This information can be included in a learning model by either enlarging the receptive field size (i.e. widening the field of view) [35, 39, 40] or by incorporating context-aware features that encode neighboring information into the target object [41] (i.e. a specific tree in forestry applications). However, context-based studies typically rely on deep learning architectures and large datasets [35], which may obfuscate the explainability of model performance improvement, which make them suboptimal for ecological applications, where the focus is on explaining regulation factors. In contrast, when interpretability and dataset size limitations are critical, shallow learning methods (e.g. ensembles of decision trees and regularized linear models) are usually preferred [42, 43].

Here, we present a UAV LiDAR–based framework that combines ecological analysis of forest structural organisation with context-aware modelling of tree diameter and tree-level AGB across 33 ha of a mature Norway spruce forest, in near-natural conditions. We first analyse gradients in tree height across the forest to delineate tree assemblages and examine their morphology. This enabled an explicit assessment of relationships between tree-level attributes (i.e. height) and assemblage-level characteristics. Building on this structural analysis, we then evaluate whether assemblage-derived information can be leveraged to improve predictions of tree diameter and AGB. Specifically, we (i) acquired close-range UAV LiDAR point cloud data, (ii) quantified spatial associations in tree height to define tree assemblages, (iii) characterised assemblage morphology as an indicator of forest structural organisation and ecological similarity, and (iv) integrated tree assemblage metrics into pairs of twin regression methods that differ only in the use of contextual information. We assessed prediction performance across three shallow learning methods and two datasets from the same coniferous forest. The proposed approach relies exclusively on UAV LiDAR data, without ancillary information or inventory-derived metrics, facilitating practical application.

2 | MATERIALS AND METHODS

2.1 | Study Area

The Seehornwald Davos research site (46° 48’ 55.2"N, 9° 51’ 21.3" E, 1640 m a.s.l.) is located in a managed subalpine coniferous forest on the western flank of the Seehorn mountain, near Davos, in the Swiss Alps. The site is labeled as a class-1 forest Ecosystem station (CH-Dav) [44] of the Integrated Carbon Ecosystem Station (ICOS) network [45] where regular forest inventory measurements are collected following standardized protocols. The site is covered by spruce trees (proportion of *Picea abies (L.) Karst*., > 99.5 %) with an average height and age of 13 m and 84 years, respectively, while some trees reach a height of 40 m and an age of 350 years. The stand parameters at the research site include tree density: approx. 1143 tree/ha; basal area: 41.9 m^2/ha; mean crown area of dominant canopy: 13.2 m^2; and mean diameter at breast height (DBH): 17.3 cm.

The study area has not been affected by infrastructure development during the 20th-21st centuries. Since 1930, grazing livestock in the forest was abandoned, and the region is sustainably managed according to the Swiss Forest Law (1876) [46]. The history of the site [47] shows that it was selected as a research site in 1985, and there has not been management activities or harvesting in the study area, except for a clearing event in 2005 that partially affected one Sparse Measurement Plot (SP-6, Annex VI). Maps dating back to 1845 reveal minimal changes within the Davos-Seehornwald forest site, while slight effects of local harvests and regrowth can be observed at the timberline [46]. Since 2005, only minimal tree removals have taken place (ca. 6 trees along the road). Patchy vegetation (i.e. dwarf shrubs and mosses) covers around 30% of the forest floor (acidic ferralic podzols), which lies on a mixed silicious and dolomitic bedrock. The research site is part of national (LWF [48], TreeNet [49], SwissFluxNet [50]) and international research networks (ICOS [51], ICP Forests [52], LTER [53]). The study area spans over 33 ha (Figure 1, b) and the terrain conditions are representative of the Alps around the Landwasser valley, i.e. a varying steepness of 23 ± 14°. The site lies on the eastern flank of the valley, so most of the slopes face west-southwest (mean slope aspect is 230° SW).

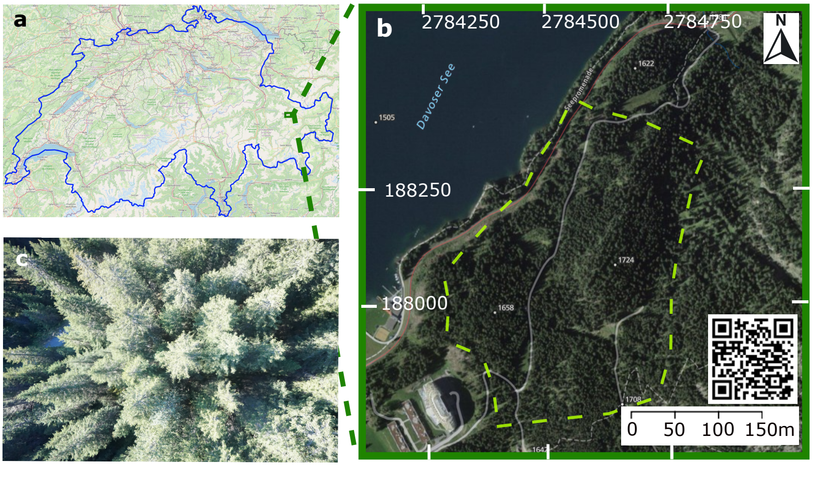

FIGURE 1 **a:** Location of the study site; the blue outline delineates the national territory of Switzerland (adapted from open.sourcemap.com). **b:** Orthoimage of the study site (adapted from swisstopo.admin.ch); coordinate units are in m, with LV95 as the projected reference system; the QR code links to additional information of the study site. The dashed yellow line shows the boundaries of the study area. **c**: Sample photo from UAV.

2.2 | UAV LiDAR Survey and Field-Based Measurements

We used a UAV-borne LiDAR system mounted to a DJI Matrice 600 Pro payload at a 90° pitch angle, and same heading and roll as the UAV platform. The system included a discrete return infrared LiDAR scanner (M8 sensor, Quanenergy Systems, Inc. Sunyvale, CA, USA) and the corresponding state-of-the art inertial and navigation systems. In addition, we used a ground based Global Navigation Satellite System (GNSS, Trimble R8) during the UAV LiDAR survey, set up in post-positioning kinematic (PPK) mode, which logged real-time satellite coverage (cf. Revenga et al. 2022 [54] for details on the airborne and ground system). The coupling of the satellite coverage data with the UAV-based laser and navigation data allowed the generation of georeferenced point clouds, following Davidson et al. (2019) [55].

Data were acquired with a UAV flight height adapted to the terrain and tree height (Figure 2, a), ensuring a >20% overlap between individual LiDAR scans of approx. 50 m width and 250 points/m^2. For each flight, the survey was performed at a fixed height above the take-off point. The surveys were conducted in October 2021, coinciding with the end of the growing season. Figure 2 (a) shows the trajectories of the UAV LiDAR flights during the survey campaign. While the standard survey coverage followed a regular auto-pilot flight grid, certain flight lines had to be manually piloted to adapt to sudden topographic features and canopy structure. The digital elevation model of the study area is provided in Annex VI, to help understand differences in flight heights.

The field-based measurements (shown in Figure 2, b) are taken on a yearly basis as part of a long-term ecosystem monitoring initiative—jointly organized by ICOS [51] and the Swiss Federal Institute for Forest, Snow and Landscape Research (WSL) [48]. Following a standardized protocol [56], expert field workers monitor tree crown status, focusing on three groups of indicators: variations in size, density and color. The number of trees that have died since the previous survey, as well as the new ones that reached a minimum DBH of 5 cm are also recorded. Tree height and DBH are monitored with a high-precision digital rangefinder (i.e. Vertex Laser Geo) and a standard calliper, respectively.

We treated two different datasets separately as ground truth measurements within the same study area: Continuous Monitoring Plot trees (CP-trees, 4 adjacent monitoring units), and Sparse Measurement Plot trees (SP-trees, 20 scattered units of 15 m radius). The two datasets (i.e. CP- and SP-trees) are monitored by different research groups on the field and protocols presented minor differences. Two main factors led us to consider both datasets separately: (i) the CP-dataset is clustered and spatially continuous, while the SP-dataset is spatially discontinuous and distributed along the study site (Figure 2, b); and (ii) the two datasets present differences in morphological trait distribution (Annex V). Figure 2 (b) shows the spatial distribution of the field-based forest inventory. The CP tree position was recorded using a Leica GPS1200 total station. The location and size of the sampling plots were defined according to ICOS protocols [57, 58]. The center location of the SP plots was determined using a GNSS Leica CS20 (antenna GS15) with a real-time kinematic (RTK) signal (accuracy measurements ranges from 0.03 m to 0.7 m). Next, the trees in the SP plots were positioned by measuring the azimuth with a field goniometer, while the horizontal distance of each tree and the inclination from the plot centers was determined using a Vertex Laser Geo meter. The accuracy of foot location of trees in the SP plots is within 0.5m and 1.2 m. The field-based inventories used as ground truth contain measurements taken between October 2019 and July 2021. The changes in structural traits between the time of field-based measurements and UAV LiDAR data acquisition were considered negligible for the purposes of this study and no major disturbance events were registered during this period.

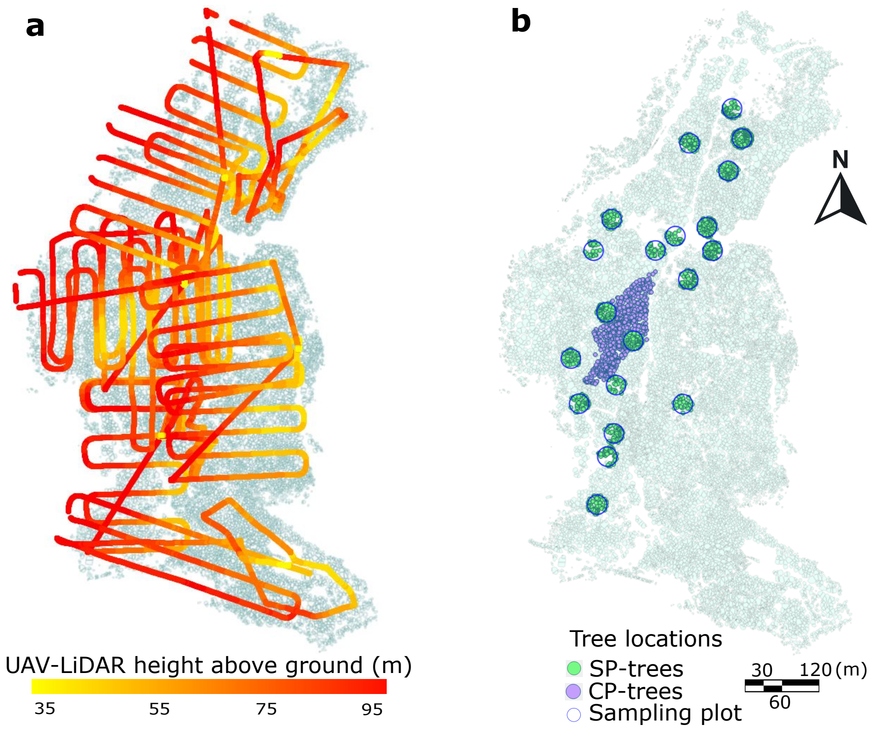

FIGURE 2 **a:** Trajectories of individual flights during survey of the Unstaffed Aerial Vehicle (UAV) Light Detection and Ranging (LiDAR) sensor; color gradient indicates height above ground during survey. Only the trajectories during LiDAR data acquisition are shown (take off and landing trajectories not shown); the flight height (fixed above take-off point) shows the difference between the horizontally stable UAV survey and the variable terrain elevation. **b:** Spatial distribution of field-based forest inventory. Dots represent the locations of the ground truth labels. The Sparse Measurement Plot-trees (SP-trees, N = 1616 trees) are shown in green; the Continuous Measurement Plot-trees (CP-trees, N = 758 trees) are shown in purple. In both **a** and **b**, the underlying polygon dataset shows the individual tree canopies after the canopy height model segmentation.

2.3 | Method setup

The workflow we followed is presented in Figure 3. Initially, the PCD generation followed the approach described in Revenga et al. (2022) [54]. The resulting PCD scene was normalized and rasterized to obtain a canopy height model (CHM), which in turn was subject to individual tree crown segmentation producing a two-dimensional polygon dataset. For the CHM segmentation, we utilized the watershed algorithm of Chen et al. (2006) [59]. The match between field-based measurements and individual tree crown polygons was conducted based on the closest distance between the field-based GNSS point measurement and the individual tree crown polygon centroid.

In order to ensure that only the LiDAR-detected trees would be accounted for in the regression experiment, a pre-processing task was required (marked * in Figure 3, the details of the preprocessing tasks involved are given in Annex II). Afterwards, using the LiDAR-derived height as polygon attribute, we calculated the distance at which the spatial autocorrelation of tree height was most significant in order to define the optimal neighborhood size (Section 3.1). Once the optimal neighborhood size had been defined, we conducted the local indicators of spatial association (LISA) analysis [60, 61] and outlier analysis [62, 63] to retrieve neighborhood metrics. Finally, two separate supervised regression experiments were performed, in order to predict DBH based on LiDAR-derived metrics: one including the neighborhood metrics (context-aware regression), the other without taking those metrics into account (context-unaware regression). Finally, AGB was estimated from the predicted DBH via an allometric function (as defined in Eq. 5).

In parallel, we evaluated the morphometry of the tree assemblages. Prior to the morphometric analysis of tree assemblages, a second pre-processing task was conducted on the individual tree crown dataset, where single crowns were merged, and inner borders were discarded (Annex II).

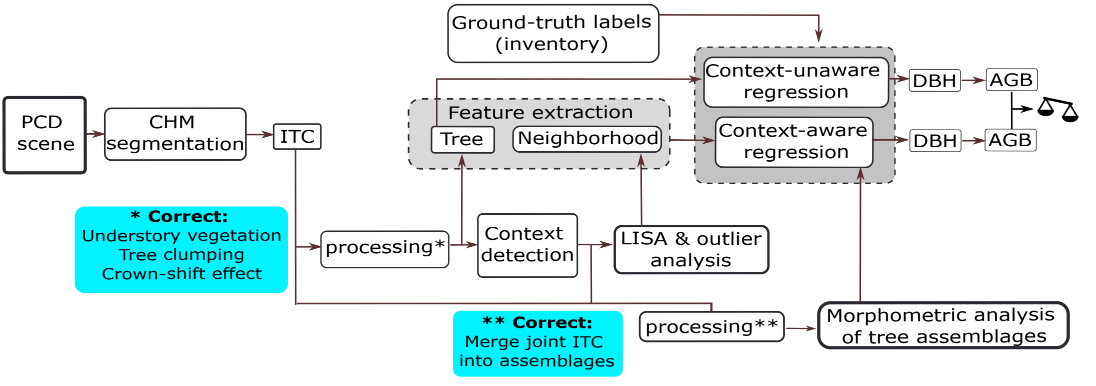

FIGURE 3 Workflow followed in this study. PCD: point cloud data, CHM: canopy height model, ITC: individual tree crown, LISA: local indicators of spatial association, DBH: diameter at breast-height, AGB: aboveground biomass. The two blue boxes describe the subtasks constituting each of the processing steps, marked * and ** in the diagram.

| Defining Spatial Context from Tree Heights

We determined the distance at which neighborhood metrics should be calculated (i.e. how many surrounding trees should be accounted as neighbors) based on local similarity of tree height. Accordingly, the selection of an appropriate neighborhood size around each individual tree (i.e. context detection) was calculated through the analysis of spatial autocorrelation of tree height as function of incremental distance. Based on the global peak in the significance of spatial autocorrelation, we defined a characteristic distance within which all included trees should be considered as neighbors. Then, all so-defined neighbor trees were accounted for to compute context-aware metrics.

This context information was encoded as metrics derived from the distance-weighted individual tree heights in each neighborhood, calculated at each tree location. Specifically, the metrics computed to define the local context were: local Moran's *I* (i.e. an estimate of local significance of tree height similarity with respect to the global variance); and spatial lag of tree height (i.e. a weighted average of heights calculated entirely locally) [64].

Local Moran's I_i is a well-established distance statistic in spatial data analysis [65], used for detecting local spatial autocorrelation and included within the family of LISA methods [60, 61, 64]. Similarly to other geostatistics methods [66], it relates attribute similarity with locational similarity, mapping autocorrelation across the geographic space. In the following definitions, σ is the global sample standard deviation of tree height; n and m represent the total number of instances (i.e. all trees in the forest) and the number of neighbors to each tree, respectively; y_i indicates the magnitude of interest at a particular point of interest (i.e. tree height) while the overline (i.e. $\overline{y}$) indicates the global average; $w_{i,j}$ indicates the distance weighting of each neighboring tree (here defined as inverse distance weighting); subindexes i and j indicate the tree of interest and a neighbor tree, respectively. Let $y_1, \ldots, y_n$ be the tree height values of all the n trees in the dataset. Then, the Local Moran's I_i [60] is defined as

$$I_i = \frac{y_i - \overline{y}}{\sigma^2} \sum_{j \in \mathcal{N}_i, j \neq i} w_{i,j} (y_j - \overline{y}), \tag{1}$$

where $\mathcal{N}_i \subset \{1, \ldots, n\}$ is the set of indices corresponding to the nearest neighbors of tree $i \in \{1, \ldots, n\}$ in the overall set, where

$$\overline{y} = \frac{1}{n} \sum_{i=1}^{n} y_i, \tag{2}$$

and

$$\sigma = \sqrt{\frac{\sum_{i=1}^{n} (y_i - \overline{y})^2}{n - 1}}, \tag{3}$$

are the global average height and the global sample standard deviation, respectively. It should be noted that insofar I_i includes global metrics (such as n, σ and $\overline{y}$), it is not entirely locally computed, but may present correlation with global features (i.e. characteristics derived from the entire dataset; cf. Westerholt et al. 2018) [67].

The Spatial Lag (SL_i) of tree height for a tree i is a spatial smoother defined as

$$SL_i = \sum_{j \in \mathcal{N}_i, j \neq i} w_{i,j} y_j \tag{4}$$

where the elements of the spatial weights matrix ($w_{i,j}$) are row-standardized, so that $\sum_{j \in \mathcal{N}_i, j \neq i} w_{i,j} = 1$. Therefore, SL_i can be seen as a weighted average of the heights of neighboring trees [68].

The neighborhood metrics finally chosen as context-aware predictors are the following: local Moran's Index (I_i), z-score of I_i, p-value of I_i, z-transformed value of I_i and SL_i—computed at 20 m, 30 m , 40 m and 50 m distance bands. Additionally, the mean heights of the k-nearest trees, with k $\in (5 - 75)$, were also included as predictors. Likewise, we also included the topographic wetness index (TWI) [69] in order to evaluate the relative predictive performance of neighborhood metrics with respect to a well-established environmental variable as tree-growth predictor [70] (Annex VII).

Finally, we included in the regression experiments predictive features informing of local neighbor dissimilarity, i.e. local outliers of tree height. We detected local outliers using Local Outlier Factor [62] and Isolation Forest [63] algorithms. The evaluation of these features allowed us to discern between the contribution of local similarity features (i.e. Local Moran's I_i and SL_i) and that of the local outliers.

Forest Structure

In order to define the tree assemblages, both local Moran's I_i and SL_i were computed at the optimal distance band to obtain neighborhood metrics, i.e. based on the global peak in the significance of spatial autocorrelation of tree height as a function of distance (using ArcGIS Pro) [71].

Tree assemblages were therefore defined as geographically continuous groups of trees delineated according to either (i) variation of local Moran's I_i of tree height, or (ii) according to quantiles of SL_i of tree height. The rationale for using two different statistics to calculate tree neighborhood metrics and thus delineate different tree assemblages is that while SL_i is entirely locally calculated, local Moran's I_i includes global features (and is therefore sensitive to the statistical characteristics of the dataset as a whole, Section 2.3). In order to discern which of the two approaches resulted most convenient in delineating tree assemblages (the former *entirely* local; the latter only *partially* local), both were included.

Tree assemblages defined according to local Moran's I_i are geographically continuous groups of trees with significantly different heights than the global tree height average, and they also lie in a region with significantly different neighbors. Local Moran's I_i identifies regions where the clustering of either high or short trees occurs. In the standard notation [64] (i.e. *High-High* or *Low-Low*), the first term refers to the individual tree and the second to the neighborhood (e.g. a tree belonging to a *High-High* assemblage is a "significantly high tree" in a "significantly high neighborhood"). The areas not showing statistical significance (a p-value ≥ 0.002 was considered sufficient) were labeled as *Not-Significant*. The significance test is based on random permutations (n = 499) of neighboring tree-height values at each step in the computation. The number of permutations and p-value indicate that, under the null hypotesis (i.e. tree heights being randomly distributed), a single tree canopy may be wrongly classified with a probability of 0.002, which was deemed sufficient for the purpose of evaluating tree assemblage morphometry (i.e. if 1 out of 499 trees is wrongly attributed to a neighborhood, the morphometry of the assemblage will not change markedly). Then, for every permutation, a local Moran's I_i value was calculated by randomly rearranging the tree heights of neighboring values. The result is a randomly generated reference distribution of expected local Moran's I_i that is compared against the observed local Moran's I_i (Eq. 1) [61]. In this way, tree assemblages defined according to local Moran's I_i are classified as: *High-High*, *Low-Low*, or *Not-Significant*.

Likewise, tree assemblages defined according to SL_i of tree height are geographically continuous groups of trees delimited according to the local weighted average of tree height [68], as defined above (Eq. 4). For the purpose of this study, 5 subdivisions based on quantiles were deemed convenient, rendering a classification of tree assemblages based on SL_i ranking as: *Highest*, *High*, *Mid*, *Low* and *Lowest*.

The morphometric analysis examined the outer boundaries of the tree assemblages as defined above. Twenty basic morphometric parameters as well as 20 derived parameters were calculated for each type of tree assemblage. The 20 basic morphometric variables are simple parameters obtained by fitting elemental geometric shapes to each tree assemblage polygon (e.g. area of maximum inscribed circle), and basic positional parameters (e.g. XPOL, which is the X coordinate of the centroid of the tree assemblage polygon). The 20 derived parameters are adimensional metrics (except for concavity [72], measured in m) computed from the 20 basic morphometric variables, as explained in Güler et al. 2021, [73] (Annex III). The morphometric analysis of tree assemblages was conducted using PolyMorph-2D algorithm, available as a plug-in for the open source JumpGIS software [74].

| Regression Models Selected

The regression experiments were designed to predict DBH, since AGB is a variable determined by the combination of DBH, height and wood density [9]. In contrast, DBH is directly measured in the field, which makes it a better defined regression target. Therefore, the model estimates of AGB were derived from the DBH prediction outputs by means of an allometric fit (Eq. 5). Predicting DBH, instead of AGB directly was chosen as more suitable, as it avoids burdening the learning models with the statistical error contained in the allometric fit. Three feature-based shallow learning regression methods were selected: namely AdaBoost [75, 76, 77], Lasso [78] and Random Forest [79] regressors. The AdaBoost regressor is a tree-based gradient-boosting method that relies on stage-wise additive expansions. Its effectiveness stems from combining weak learners to form a generalized prediction hypothesis. Random Forest is a well established tree-based ensemble regression method. Finally, Lasso is a linear model that applies an L1-norm penalty for regularization [80]. In our case, all three shallow regression methods utilize the features derived from the individual tree crown polygon dataset resulting from the CHM segmentation.

Context-unaware regressions were defined as those in which a learning model performs DBH regression by taking as predictors only individual tree attributes derived from the ITC polygon dataset (i.e. tree height, canopy area and canopy perimeter), as it is a common approach [8]. On the other hand, we defined context-aware regressions as those regressions in which contextual features are additionally introduced as predictors. These were either neighborhood metrics (e.g. SL_i of tree height) or TWI at different spatial resolutions (Section 2.3) . For every model predicting DBH from individual tree attributes (i.e. context-unaware conditions) we implemented a context-aware counterpart. This allowed us to evaluate the impact of context on regression performance.

| Model Training and Validation of Results

A direct validation of AGB is not possible without harvesting trees destructively, which raises obvious ethical, legal and economic issues. Instead, non-invasive methods that use remote sensing data and allometric functions are the standard procedure for estimating AGB [57]. Here, we estimated AGB from tree height, DBH, wood density and an allometric function of Norway spruce trees (Eq. 5). Therefore, the regression analyses conducted focused on comparing performance of predictions on DBH between twin shallow learning methods (i) "context-unaware" and their (ii) "context-aware" counterparts. As independent ground reference to compare against, we used inventory-based DBH.

We chose DBH as the variable to test model predictions, which is included in the field-based forest inventory, and therefore directly measured by *in situ* monitoring. Next, in order to assess the benefits of including context in the regression models, we compared results using AGB of individual trees. Specifically, AGB estimates were derived via species-specific allometric and wood density functions, tree height retrieved via UAV LiDAR, and DBH predicted via

ML regression. The allometric model used was the one proposed by Dalponte and Coomes (2016) [9]:

$$AGB_{tree} = \alpha \cdot WD_{spruce}^{\beta} \cdot (DBH - d_0)^{\gamma} \cdot H^{\delta}, \tag{5}$$

where the wood density value (WD_{spruce}) was taken from Alpine spruce dendrometric models [81], *DBH* was predicted via ML regression and height (*H*) was extracted from the UAV LiDAR acquisition. $\alpha, \beta, \gamma, \delta$ and d_0 are species-specific fitted allometric parameters [82], obtained from allomeric fits to harvested spruce trees by the Forestry and Wildlife Service Agency of the province of Trento (Italian neighbouring province southeast from the study site, also used in Dalponte and Coomes, 2016), and we consider them applicable to the Seehornwald Davos research site. At all events, for the purpose of assessing the benefits of a context-aware approach, the specific characteristics of the allometric fit used are negligible, as it is only used to quantify a difference in terms of AGB, and both types of predictions (in either aware or unaware conditions) take the same equation. Therefore, the predicted value of DBH was input into Eq. 5, in order to obtain model predictions of AGB. This allowed to compare AGB predictions with the ground truth values of AGB, which were similarly obtained via the field-based measurements of DBH and height (provided by the regular tree-monitoring campaigns of ICOS [51] and WSL [48]), and Eq. 5.

The technique used to estimate model prediction error consisted of a nested cross-validation (NCV, Annex IV) scheme adapting the procedure from Bates et al. (2021) [83]. Following the NCV scheme, the dataset was partitioned into 10 random outer folds, which are mutually exclusive. For each outer iteration, one outer fold was held out as an independent test set, while the remaining nine folds formed the training set. This training set was further partitioned into 5 mutually exclusive inner folds, over which a 5-fold cross-validation was performed to tune model hyperparameters and select the optimal model configuration. Inner-fold validation performance was used exclusively for model selection, while performance obtained on each outer test fold was retained as an independent estimate of generalization error. The model inspection technique used to evaluate predictors' influence on the DBH regression results was the permutation importance method as proposed by Altmann et al. (2010) [84]. Permutation importance was computed on the outer test folds only, to avoid information leakage. The feature-elimination procedure consisted of eliminating progressively those predictors that presented a negative mean importance, with feature removal performed within the NCV training process, as they were considered harmful to the model's performance. The significance of the enhancement in context-aware predictions and effect size was assessed using Wilcoxon signed-rank test [85] and Cliff's Delta analysis [86], respectively. Outer-fold performance scores were treated as paired samples, forming empirical performance distributions for the context-unaware and context-aware models, respectively. Statistical tests were applied to these paired outer-fold results, using corresponding folds as matched observations.

3 | RESULTS

3.1 | Context Detection and Forest Structure

The analysis of spatial autocorrelation of tree height as function of incremental distance resulted in a maximum significance at a distance of 40 m. Figure 4 (a) shows the calculation of local Moran's index (I_i) of tree height at different distance bands. Figure 4 (b) shows the standard score (i.e. z-score) of I_i obtained at each distance band, resulting from comparing the observed I_i and the expected I_i under the tree height randomness assumption (Annex I). As a precaution, we ran context-aware regression experiments including also context features retrieved at shorter (i.e. 20

m, 30 m) and larger (i.e. 50 m) distances than the optimal range (i.e. 40 m). The context features retrieved at these distances (i.e. 20, 30, 40 and 50 m) which contributed to improve the predictions of DBH were all included in the final regression models.

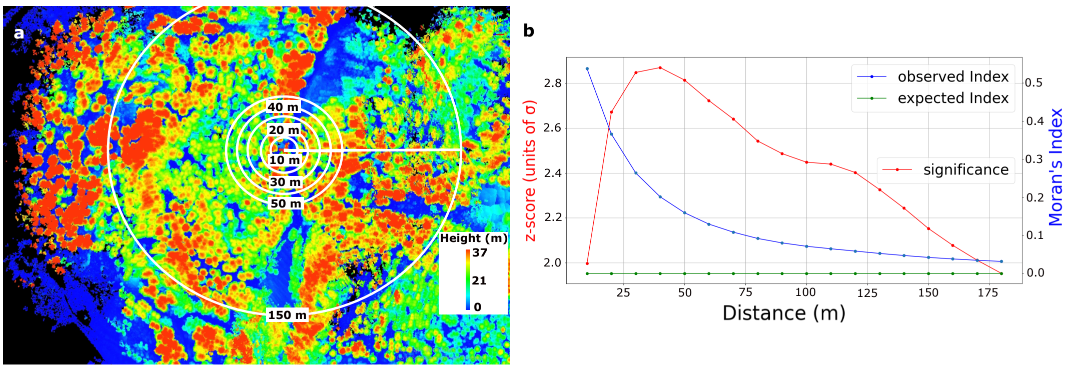

FIGURE 4 Context detection. **a:** Normalized point cloud data (PCD) scene colored by tree height overlaid with a selection of the appropriate radii for defining the neighboring context. **b:** Autocorrelation of tree height as function of distance. The red line shows the number of standard deviations (σ) that an observation is away from the expected value (under the assumption of heights being randomly distributed). The blue and green lines show the actually observed local Moran's Index and the expected value under randomness assumption, respectively.

In Figure 5, panels a and b show the spatial distribution of tree assemblages calculated using either local Moran's I_i or SL_i of tree height, respectively, at 40 m range. While both types of assemblages show similarities as regards extent, morphometry and location, SL_i captures more local variability, resulting in more small, localized clusters. This is not only due to a higher discretization (5 clusters in SL_i, vs. 3 clusters in local Moran's I_i), but also to the fact that SL_i is not sensitive to the variance in the dataset beyond the range of its neighborhood (as explained in Section 2.3).

The morphometric analysis provided 40 additional features that were evaluated as potential predictors of DBH. In Figure 6, panels a and b visualize the results of the morphometry analysis of tree assemblages defined by local Moran's I_i and by SL_i, respectively. The circular barplots show the average magnitude as bar lengths, and the standard deviation as dots. Both mean and standard deviation values are shown as min-max scaled (across assemblage types) to present all variables on the same radial axis and to ease visual comparison, i.e. for every morphometric variable, the highest value is replaced by 1, the minimum is replaced by 0, and the intermediate values are linearly interpolated between 0-1. It can be observed that the morphometric variables follow very similar trends when tree assemblages are defined based on local Moran's I_i or SL_i. However, an observed difference between SL_i and local Moran's I_i was found in the heteroscedasticity of the morphometric variables calculated, where only in the former case variance of all metrics scaled with magnitude.

While not for all variables a systematic trend was found, for several basic morphometric variables a linear positive correlation between them and SL_i was observed, as shown by the Pearson coefficient (ρ). This is the case for polygon area (ρ= 0.95), perimeter of polygon (PPOL; ρ=0.98) and radius of the minimum circumscribed circle (RMCC; ρ=0.98). Additionally, a positive correlation was found for some derived morphometric variables, namely: length-to-width ra-

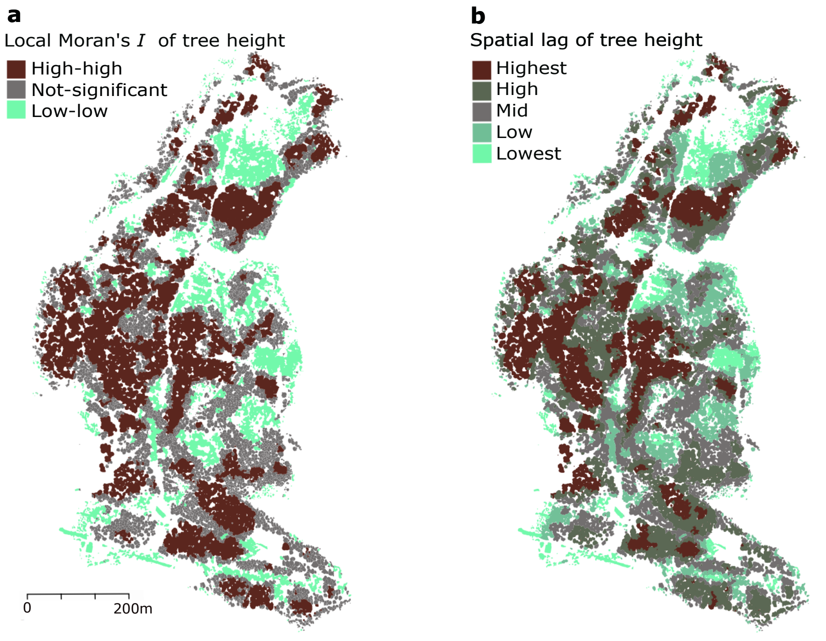

FIGURE 5 Tree assemblages defined by local similarity of tree height. **a:** Delineated according to local Moran's I_i of tree height. **b:** Delineated according to spatial lag of tree height (SL_i).

tio (LTWR; ρ=0.75) [87], circularity ratio (CIRR; ρ=0.88) [90], compactness factor (COMF; ρ=0.89) [73], dispersion measure (DISM; ρ=0.90) [90], complexity index (COMI; ρ=0.88) [73], lemniscate ratio (LEMR; ρ=0.81) [94], regularity factor (REGF; ρ=0.82) [89], and concavity (CONC; ρ=0.96) [72]. Conversely, other morphometric variables showed a decreasing trend with increasing SL_i. A clearly negative correlation between SL_i and the following derived morphometric variables was found: Miller's circularity ratio (MCIR; ρ=-0.88) [92], Horton's form factor (HFOR; ρ=-0.88) [87], elongation factor (ELOF; ρ=-0.83) [93], shape factor (SHAF; ρ=-0.95) [89], rectangularity (RECT; ρ=-0.85) [97] and roundness (ROUN; ρ=-0.69) [95]. More details are given in Annex III (Figure 12).

3.2 | Tree diameter Regression: Aware vs. Unaware of Local Context

Regression experiments including context-aware features improved predictions of DBH consistently (Figure 7, Tables 1 and 2), resulting in enhanced tree-level AGB predictions via allometry (Eq. 5). We found a general trend across methods of improved prediction performance w.r.t R^2, RMSE and MAE in both SP- and CP-datasets. For each pairwise comparison, the improvements were consistent, although the degree of prediction enhancement differed between the two datasets considered. Predictions in the CP-dataset observed a lower enhancement in comparison to predictions in the SP-dataset. For instance, with AdaBoost, RMSE was reduced by 4.1% (SP-dataset) vs. 0.8% (CP-dataset), with corresponding improvement observed in R^2 values, i.e. by 0.03 (SP-dataset) vs. 0.024 (CP-dataset). This contrast between the sparse (SP) and continuous (CP) datasets suggests that the lower contextual variability in the CP dataset limits the added value of context features, whereas higher contextual variability in the SP dataset makes their contribution more effective.

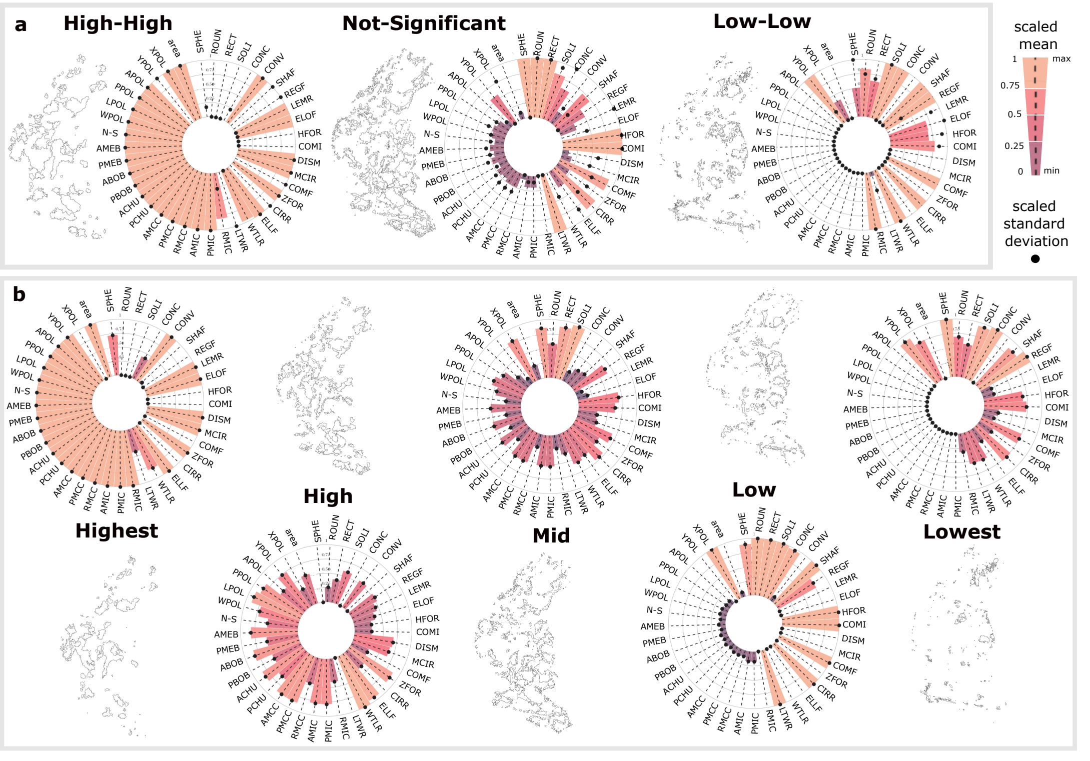

FIGURE 6 Morphometric analysis of tree assemblages grouped by **(a)** local Moran's I_i, and **(b)** by spatial lag of tree height. Bar length and color gradient represent the mean value, while black dots represent the standard deviation (SD) over all tree assemblages. Both mean and SD are scaled (min-max) to allow comparison of all metrics across assemblage types on the same axis—i.e. for every morphometric variable, the highest value of a certain assemblage type is replaced by 1, the minimum value is replaced by 0, and the intermediate values are linearly interpolated in between the range (0-1). YPOL: northing of centroid of the tree assemblage; XPOL: easting of centroid of the assemblage; APOL: area of polygon (P); N-S: defined as $|sin(azimuth)|$, shows the alignment of the main axis of P with the North-South direction; PPOL: perimeter of P; LPOL: major axis length (L) of P; WPOL: minor axis length (W) of P; ABOB: area of the bounding box fully containing P; PBOB: perimeter the bounding box fully containing P; AMEB: area of the minimum enclosing box fully containing P; PMEB: perimeter of the minimum enclosing box fully containing P; ACHU: area of containing hull ; PCHU: perimeter of convex hull fully containing P; AMCC: area of the minimum circumscribed circle (MCC); PMCC: perimeter of MCC; RMCC: radius of MCC; AMIC: area of maximum inscribed circle (MIC); PMIC: perimeter of MIC; perimeter of MCC; RMIC: radius of MCC; LTWR: length-to-width ratio [87]; WTLR: width-to-length ratio [88]; ELLF: ellipticity factor [89]; CIRR: circularity ratio [90]; ZFOR: Zavoianu's form factor [91]; COMF: compactness factor [73]; MCIR: Miller's circularity ratio [92]; DISM: dispersion measure [90]; COMI: complexity index [73]; HFOR: Horton's form factor [87];ELOF: elongation ratio [93]; LEMR: lemniscate ratio [94]; REGF: regularity factor [89]; SHAF: shape factor [89]; CONV: convexity [95]; CONC: concavity [72]; SOLI: solidity [96]; RECT: rectangularity [97]; ROUN: roundness [95]; SPHE: sphericity [98]. Correlation coefficients of the most prominent variables are given in Annex III.

Figure 8 (a) shows the ground truth labels (i.e. field based estimates of AGB), which were derived from the field measurements and the allometric fit (Eq. 5). The central panel (b) shows the spatial distribution of residuals (i.e. $\epsilon = AGB_{ground.truth} - AGB_{prediction}$) of the AdaBoost context-aware regression results (i.e. the best perfor-

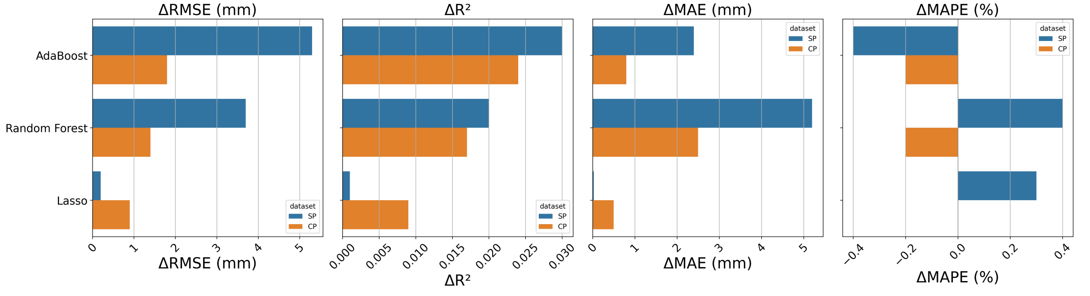

FIGURE 7 Enhancement of predictions of diameter at breast height per model type as a result of including context-based predictor variables (zero-reference corresponds to the prediction performance without including context-based predictors). MAPE: mean absolute percentage error.

mance). The mean values converge towards zero (i.e. $\bar{\epsilon}_{SP} = 3.8$ kg , $\bar{\epsilon}_{CP} = -3.2$ kg), while the spread of the error distribution varies between SP and CP-datasets (i.e. $\sigma(\epsilon_{SP}) = 123$ kg, $\sigma(\epsilon_{CP}) = 140$ kg). Figure 8 (b) also shows a low spatial autocorrelation of errors (i.e. low clustering of errors), indicating that predictions are not geographically biased. Figure 8 (c) displays the error distributions in both datasets. SP-errors show a unimodal distribution with a slight over-estimation of DBH of 28 mm. CP-errors present a similar overestimation bias (25 mm) with a bimodal distribution (the second mode is located at 25 mm of underestimation). The second mode of the bimodal pattern in the CP-dataset may correspond to the more frequent occurrence of larger trees, which tend to be underestimated (Figure 8, c, lower panels). It can be observed that, generally, smaller and thinner trees tend to be slightly overestimated (i.e. in the first two quantiles) compared to the largest trees, which tend to be underestimated.

Figure 9 presents the analysis of the relative importance of all predictors considered in the context-aware DBH regression with the AdaBoost regression model. The analysis reveals that in both SP- and CP-datasets, the most important context-based predictors are the average heights of the 5, 10, and 15 nearest neighboring trees, outperforming some individual-tree metrics, such as the crown metrics.

TWI made a marginal contribution to enhanced predictions, which was less than that of any neighborhood metric. Moreover, although modest, TWI exhibited a greater impact on improved predictive performance at finer spatial resolutions in both datasets (Figure 9), whereas its contribution decreased at coarser resolutions.

TABLE 1 Results (on test set) of the SP-dataset, for each pairwise model comparison (aware vs. unaware of context features). Predictor variables are entirely LiDAR-derived; the target variable is diameter at breast-height (DBH, in mm). The values are presented as mean ± standard deviation of the 10 outer CV folds of the nested scheme. One asterisk (*) marks results where the enhancement introduced by context-awareness is statistically significant with "small" size effect, while ** and *** mark "medium" and "large" size effect, respectively. The best results are shown in bold. RMSE (%) is the error relative to the median DBH (125 mm). MAPE: mean absolute percentage error.

Regression model	R^2	RMSE (mm) / %	MAE (mm)	MAPE (%)
AdaBoost (unaware)	0.830 ± 0.05	58.0 ± 9.0 / 46.4 ± 7%	43.3 ± 4.4	19.1 ± 1.9
AdaBoost (aware)	**0.860 ± 0.03** ***	**52.7 ± 5.3** *** / 42.1 ± 4%	**41.0 ± 3.1** **	**19.5 ± 1.7**
Random Forest (unaware)	0.818 ± 0.04	60.2 ± 7.3 / 48.1 ± 6%	46.8 ± 4.5	22.8 ± 5.8
Random Forest (aware)	0.838 ± 0.05 *	56.5 ± 9.2* / 45.2 ± 7%	41.6 ± 5.4 ***	22.4 ± 5.1
Lasso (unaware)	0.851 ± 0.02	54.6 ± 4.9 / 43.6 ± 4%	4.20 ± 3.3	19.1 ± 1.4
Lasso (aware)	0.852 ± 0.02	54.4 ± 4.9 / 43.5 ± 4%	4.17 ± 3.5	18.8 ± 1.7

TABLE 2 Results (on test set) of the CP-dataset, for each pairwise model comparison (aware vs. unaware of context features). The predictive variables are entirely LiDAR-derived; the target variable is diameter at breast-height (DBH, in mm). The values are presented as mean ± standard deviation of the 10 outer CV folds of the nested scheme. One asterisk (*) marks results where the enhancement introduced by context-awareness is statistically significant with "small" size effect. The best results are shown in bold. RMSE (%) is the error relative to the median DBH (220 mm). MAPE: mean absolute percentage error.

Regression model	R^2	RMSE (mm) / %	MAE (mm)	MAPE (%)
AdaBoost (unaware)	0.713 ± 0.07	54.7 ± 5.98 / 24.8 ± 3%	43.0 ± 5.26	15.5 ± 2.4
AdaBoost (aware)	0.737 ± 0.05 *	52.9 ± 5.28 * / 24.0 ± 2%	42.2 ± 4.43 *	15.7 ± 3.1
Random Forest (unaware)	0.688 ± 0.07	57.0 ± 5.9 / 25.9 ± 3%	43.8 ± 5.1	15.7 ± 3.1
Random Forest (aware)	0.705 ± 0.04	55.6 ± 5.3 / 25.2 ± 2%	41.3 ± 5.5 *	15.9 ± 4.3
Lasso (unaware)	0.741 ± 0.09	51.3 ± 6.6 / 23.3 ± 3%	39.1 ± 5.2	13.6 ± 1.6
Lasso (aware)	**0.750 ± 0.08**	**50.4 ± 5.9** / 22.9 ± 3%	**38.6 ± 4.1**	**13.6 ± 1.1**

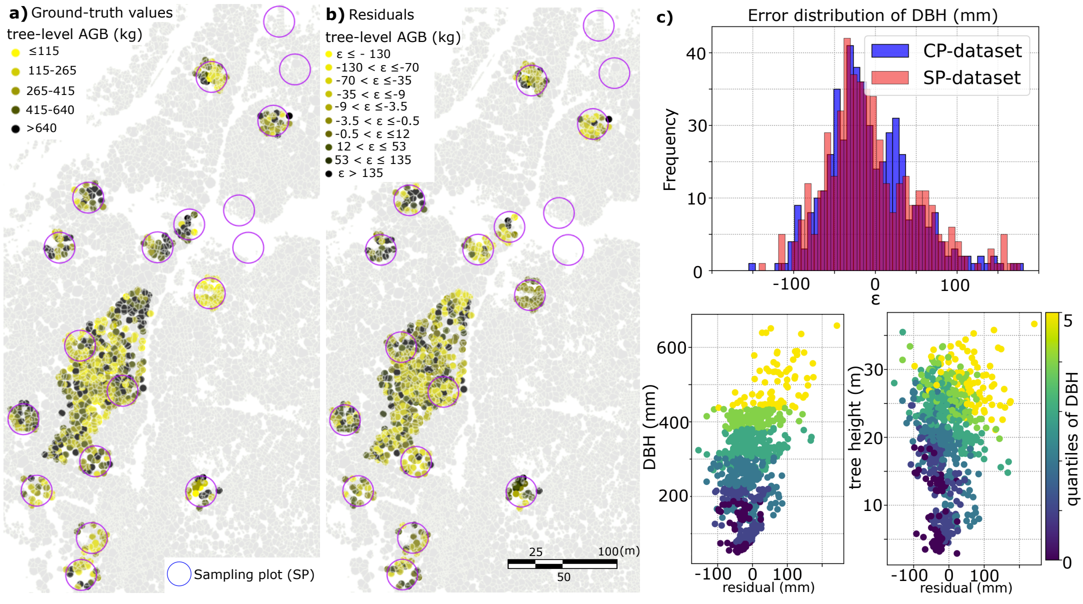

FIGURE 8 **a**: Spatial distribution of tree-level aboveground biomass (AGB) according to ground truth measurements. **b:** Spatial distribution of residuals ($\epsilon = AGB_{ground-truth} - AGB_{prediction}$) of AGB predictions with AdaBoost context-aware regression, grouped by quantiles (negative values indicate overestimation). The four empty SP-plots (and the southernmost one not included) correspond to areas where the quality of the UAV LiDAR data collection was compromised (Annex VI). **c**: Error distributions of diameter at breast-height (DBH) in Sparse Measurement Plot (SP) and Continuous Measurement Plot (CP) datasets. The two bottom-right panels show the residual distribution of DBH (in x-axis) vs. field-measurements of DBH and tree height (in y-axes). The color scheme refers to the quantiles of each dataset separately, which are differently distributed (Annex V).

4 | DISCUSSION

4.1 | Forest Structure

The analysis of morphometric variables for different tree assemblages (Figure 6) permitted to examine whether trees—grouped by local association of tree heights—persistently show different shapes at the group level, shedding light on the relationship between context-based traits (e.g. concavity of a tree assemblage) and single-tree heights. This analysis revealed certain patterns of trait convergence [99], which was specially remarkable for some metrics, which showed a strong correlation with tree height (e.g. concavity [72] and length-to-width ratio [87]).

Remarkably, it was observed that tree assemblages delineated according to the spatial lag of tree height (i.e. SL_i, Figure 6, b) presented clear positive correlations with two-dimensional morphometric features at the tree assemblage level. For instance, assemblages with higher trees (i.e. labeled as *Highest* according to SL_i, or *High-High* according to local Moran's I_i) are consistently rounder, larger and more regular in shape. As visualized in Figure 6, SL_i correlates positively with shape regularity [89], concavity [72], length-to-width ratio [87] and size, indicating a consistent trait-convergence assembly pattern. Higher trees tend to converge in most sheltered areas (i.e. thalwegs and local sub-basins) so that tree assemblages with highest SL_i tend to adopt the morphological features of the drainage net-

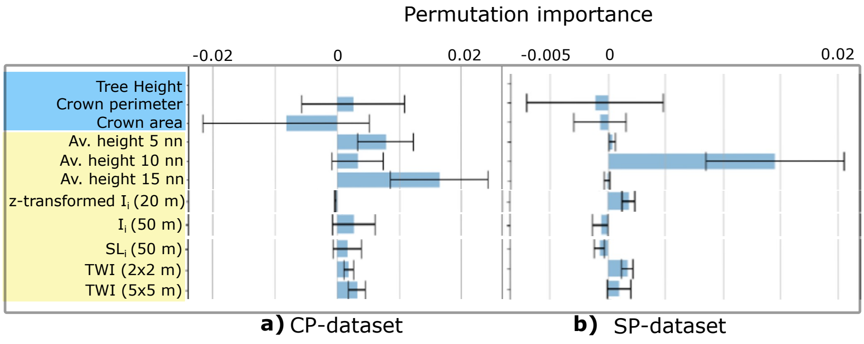

FIGURE 9 Inspection of predictors' permutation importance [84] in the AdaBoost regression experiment in context-aware conditions. The left panel **(a)** shows results in the control plot (CP) dataset, and the right panel **(b)** shows results in the Sparse Measurement Plot (SP) dataset. Bar length and error bar show the mean and standard deviation of a predictor's importance, respectively. Predictors highlighted in blue are individual tree traits; predictors highlighted in yellow are context-based. In both datasets, it can be noted how the average heights of the 5-15 nearest neighbors (nn) stand out as the strongest predictors, outperforming crown perimeter and crown area. In both plots (**a** and **b**), individual tree height (with importance: 0.85 in CP-dataset; 1.3 in SP-dataset) has been removed to facilitate visual comparison of the remaining predictors. Only the 10 most significant predictors are included; an extended figure is shown in Annex VII.

work's shape (Annex III). A more detailed interpretation of this observation, particularly in relation to tree assembly morphology, would warrant a dedicated follow-up study. However, it may indicate that both the shape and location of tree assemblages of different heights are conditioned by underlying environmental and biotic driving mechanisms.

In the coniferous forest studied here, a significant degree of clustering of tree heights takes place (Figure 5, a), while spatial gradients of tree height present preferential shapes and directions (Figure 5, b). These observations indicate that there is tree-height convergence and a tendency toward optimal phenotype expression (i.e. maximum growth performance) around the runoff drainage network (Annex III, Figure 10). Higher trees are found in sheltered regions and concave channels—which generally benefit from more frequent runoff events and deeper soils [100, 101]. This may indicate that favorable environmental conditions (e.g. deeper soil, lower soil moisture recession rates, greater availability of soil nutrients due to leaching) allow individuals to reach their optimal phenotype. Conversely, a lower SL_i of tree height in more exposed terrain (e.g. ridges, hilltops) may indicate that environmental filtering (e.g. windstorm disturbance) or a reduced competition for light could play a significant role in determining the location of low SL_i tree assemblages. Thus, the relatively reduced tree height in exposed areas could indicate a passive adaptation of tree height to harsher environmental conditions [102], an active adaptation to higher light availability [103], a limitation to tree growth caused by other local factors, such as lower soil depth or nutrients availability [1, 101], or the effect of these factors combined. Nevertheless, we cannot provide an interpretation of such observations, as shifts in the variance of functional traits across environmental gradients, such as gradients of tree heights, do not bring strong evidence of either biotic or environmental filtering on their own [104].

4.2 | Enhancement of Tree Diameter and Aboveground Biomass Regression

Our context-aware shallow regression approach improved estimates of tree diameter and AGB in the studied subalpine coniferous forest using UAV LiDAR data. These findings are consistent with established context learning literature [36, 37, 38, 39, 40, 41], remote sensing trait mapping studies [17, 35], and methodological advances on forest modelling—namely, nonlinear mixed-effects methods [18, 19] and competition-based studies [20, 21, 22]. We further extend this approach to a framework native to UAV LiDAR systems. The pairwise comparison of methods consistently showed that context-aware regressions outperformed context-unaware regressions across models (except for Lasso in the SP-dataset, where performance stagnated, Tables 1 and 2), and in no case adding context information became detrimental. This finding may indicate that gradients in tree heights across the ecosystem proxy for environmental and biotic mechanisms (e.g. windstorm disturbance, nutrient and soil moisture abundance, light harvesting competition) [103, 105] that influence tree growth, and can therefore be leveraged to enhance predictions at the single tree level. The results showed a consistently improved performance in tree diameter and AGB prediction when including context. The improvements were tested as statistically significant in four of the six pairwise experiments, with size effect raging from small to large. Nevertheless, none of the morphometric variables obtained from the tree assemblage analysis proved useful to improve predictions of tree-level DBH.

The Norway spruce forest under investigation exhibits a heterogeneous structure, with tree heights varying markedly across space (Figure 5). Consequently, the UAV LiDAR survey produced a heterogeneous dataset [106], a well-known challenge for automated tree phenotyping and functional trait mapping using ML methods [35]. The accuracy enhancement gained from including context-aware features in the regression experiments varied between the two datasets considered (i.e. SP-trees and CP-trees). Context-aware regressions of DBH in SP-trees experienced greater enhancement than in CP-trees. This is consistent with the fact that the CP-dataset contains less variability of context, since it is a locally clustered and more homogeneous dataset (Figure 2, b). As SP-trees are grouped in scattered plots across the forest, their spatial distribution spans hundreds of meters, making them subject to a more diverse context than the very local CP-dataset.

4.3 | The Role of Neighboring Context in Regression Performance

Most shallow learning methods achieved enhanced predictions when contextual information was included, with results consistently showing no deterioration (Tables 1 and 2), which indicates that even weak correlations could be leveraged. The average heights of the 10 and 15 nearest neighbors were the most important context based predictors for SP- and CP-trees, respectively (Figure 9). Moreover, the degree of local similarity of tree height (i.e. SL_i, local Moran's I_i) was most important and, to a lesser extent, the LiDAR-based TWI, indicating that although TWI may be a good predictor of tree growth [70], the neighborhood information resulted more useful, in agreement with previous literature [24]. In contrast, including features informing about neighbor dissimilarity, such as local outliers of tree height detected using Local Outlier Factor [62] and Isolation Forest [63] algorithms did not result in enhanced predictions (thus not shown here). We hypothesize that metrics containing information about the degree of local similarity may reveal the combined effect of ecological processes that are specific to the immediate neighboring context. In contrast, metrics that proxy for dissimilarity do not help to uncover such processes, although they remain useful in detecting outstanding trees (i.e. local outliers).

Context-based features at closer distances generally showed larger predictive power but also larger variance (as less neighboring trees were computed). For instance, the p-value of Local Moran's I_i at a 20 m range in the CP-dataset has an average positive effect but is not a stable predictor (Figure 9, a). This can be observed in the general trend of larger standard deviations in the permutation importance of predictors retrieved at short ranges than at greater distances (Annex VII). In accordance with competition-based studies [20, 21, 22], we observe that the strongest context-based predictors are those retrieved from the immediate neighboring trees in both datasets, i.e. the average height of 5, 10 and 15 nearest neighbors. However, our method additionally allows to compare the relative importance of competition-derived metrics and other context-based metrics operating at larger scales. For instance, in Figure 9 (a) it is shown that local Moran's I_i retrieved at a 50 m range is comparable in importance to the average height of the closest 10 neighboring trees A general difference observed between the CP and the SP-datasets is that the predictors' importances in the CP-dataset fluctuate more (i.e. larger standard deviations). Further, in the SP-dataset, predictors rarely become negative and if they do, it is to a lesser extent. Morphometric variables derived from tree assemblages (Figure 6) did not improve DBH predictions and were therefore excluded from the final DBH models. Accordingly, assemblage-level morphometrics are not considered further as predictive features. However, their consistent correlations with tree height were analysed separately to provide a complementary insight into forest structure (Section 4.1).

Considering context metrics to enhance estimates of DBH at the individual tree level in coniferous forests has been suggested in seminal works [26, 107] and been adopted subsequently for various applications in forest research [25, 27, 22], finding information of local context (e.g. canopy height) beneficial for e.g. wood volume and estimation of AGB components [20, 108, 109]. Moreover, recent investigations on tree morphology and productivity in coniferous forests [20, 21] have motivated the further development of competition-aware approaches to improve the prediction accuracy of individual tree traits (e.g. growth), leveraging tree canopy metrics. In forest biomass research, a commonly recognized approach is calibrating regression models with plot-level metrics for predicting tree-level structural traits (e.g. plot-level random effects in nonlinear mixed-effects methods), which has been pointed out as a methodological limitation [24]. Indeed, the results of such approaches are constrained by the artificially-delineated plot size, and it has been observed that accuracy increases with a progressively larger plot size [17, 19]. Our method to select context based on the spatial autocorrelation of tree heights (Figure 4) may indicate the range of saturation of such improvement (40 m in this study area). Furthermore, our results show that the variability and extent of context determines its beneficial leverage for prediction of tree-level traits (e.g. tree diameter, AGB).

This study continues this line of work and sheds light on how the local spatial context can be defined and leveraged in tree-level structural trait predictions (i.e. DBH), making a case for AGB estimates in a Norway spruce forest. The analysis shows that there is an optimal range to computing neighborhood metrics. In the study case considered here, this corresponded to a range including the closest 15 neighboring trees, based on the spatial autocorrelation of tree heights. Further, we found that the predictive power of context-based metrics is sensitive to context extent (i.e. the range at which such metrics are calculated). This observation may indicate that defining context based on plot-level metrics retrieved from artificially bounded units [17, 18, 19] may be seen as a constrained approach, as observed previously [24, 110]. Likewise, in the light of this observation, and in line with recent studies [111], determining the significant contextual extent of individual functional traits based on units of fixed size (e.g. pixel size) appears to be suboptimal. Therefore, future forest research would probably benefit from including context-awareness determined by spatial association of tree traits, bearing in mind that context-detection is trait-dependent and may vary depending on dataset source—e.g. spatial autocorrelation as a function of distance (Figure 4) is sensitive to CHM segmentation quality—and method applied—e.g. delineation of tree assemblages varied slightly between local Moran's I_i, and SL_i (Figure 5).

Lastly, we note that passive optical remote sensing studies usually define the optimal scale of analysis as a trade-off between the observational extent (i.e. area surveyed) and the image resolution (i.e. pixel size) [111, 112]. Also, in ecological research, it is common to subsample datasets using natural subregions based on ancillary ecological criteria (e.g. ecoregions, conservation status) [113]. Conversely, here we defined the range of influence of context-based metrics (i.e. the extent of tree neighborhoods) using a dataset-native approach, based entirely on the spatial association of individual tree heights. This permitted us to determine the context of influence unhampered by the remote sensing technique and not using external data sources. Furthermore, as local context was defined based on the spatial association of a real physical attribute (i.e. tree heights), and not defined by an artificially bounded unit (e.g. pixel size or plot size) the resulting distance could be considered characteristic of the forest ecosystem.

4.4 | Methods Applied and Limitations

We have aimed at preserving a fully-native UAV LiDAR approach, so that the applicability of the method proposed is not compromised by lacking local ancillary data (e.g. conservation status, edaphic conditions), whose availability may become a limiting factor in forest monitoring. We note that the these findings are specific to the subalpine coniferous forest considered here. Caution is advised when contemplating a direct application of this approach to more complex canopy structures and terrains, such as those found in deciduous, multilayered or broadleaf forests—. Likewise, the strength of our results is currently limited by the lack of replicates at different forest sites, so that we cannot yet confirm these findings to be generally applicable to a wider range of forest types and canopy configurations. Furthermore, the pre-processing tasks (marked * in Figure 3, Section 2.3) required as part of our experimental design, simplifies the actual LiDAR scene representing the real forest scenario. This simplification hampers a fully-automated, streamlined application, and case-specific considerations are still required.

The workflow adopted here, including the required correction steps (Figure 3), highlights three key limitations: (i) label assignment between field measurements and LiDAR-derived instances is imperfect; (ii) errors in individual tree segmentation persist; and (iii) understory trees that are not detected by UAV LiDAR are consequently excluded from the analysis. Imperfect label assignment (i) prevents a robust and automated one-to-one correspondence between measured DBH and LiDAR-derived tree height, even in this structurally simple forest. Small stem inclinations, for example, can result in crown displacements of several meters for average-height trees. Such effects are expected to become more pronounced in structurally complex or multilayered canopies. Segmentation errors (ii) primarily result in omission errors, such as multiple real trees being represented as a single LiDAR segment, which complicates label matching. In contrast, preliminary tests conducted in a broadleaf forest (Laegeren Forest Site) using the same parameterisation revealed a high prevalence of commission errors, where individual branches were incorrectly segmented as separate trees. The shift between the field-based inventory tree datasets and the UAV-LiDAR datasets (Figure 14, panels a and b, respectively, in Annex V) shows a clear thinning, particularly at the lower end of tree heights (which usually correspond to understory trees). As a result, the distribution densities of CP- and SP-datasets captured by the UAV LiDAR system, show a drift towards higher tree tops and broader stems, as the top canopy is what is being predominantly portrayed in the LiDAR scene.

These corrections may have influenced the derived context-based features, and future work could assess whether such predictors are also effective in inventory-based datasets. Nevertheless, studies using competition-based metrics [20, 21, 22] and nonlinear mixed-effects methods [17, 18, 19] indicate that the contextual information derived from plot-level metrics is informative. Here, we aimed to translate these approaches into a framework native to UAV LiDAR data, where context is not constrained by artificially delineated plot boundaries, albeit at the cost of limited understory representation. A natural extension of this workflow would integrate terrestrial laser scanning with the UAV LiDAR survey to address this limitation.

5 | CONCLUSIONS

This study introduces an integrated UAV LiDAR framework that first characterises forest structure through an ecological assessment of tree assemblage morphology, and subsequently applies context-aware modelling to improve estimates of tree diameter and derived aboveground biomass in a coniferous forest. The prediction performance demonstrated improvements in tree diameter and aboveground biomass prediction when incorporating context-aware features—the exception was the Lasso regression, which stagnated in one of the datasets considered (SP-dataset)—and in no case did contextual features have a detrimental effect. In contrast, adding morphometric variables from the tree assemblages as predictors did not enhance tree diameter prediction accuracy. The results show that the use of context-aware features as predicting variables can improve estimates of tree diameter and thus have substantial impact on AGB estimates in coniferous forests. The best performing model showed a reduction of RMSE in tree diameter predictions of 4.1% and 0.8% in the sparse (i.e. SP) and in the continuous (i.e. CP) dataset, respectively, which suggests that an heterogeneous forest context supported the regression improvements. For the best performing method (AdaBoost regression), the strongest context-based predictors were the average heights of the nearest 5-15 neighboring trees. Features that provide information about the tree neighborhood (e.g. spatial lag of tree height, average height of k-nearest trees) contain useful information (i.e. weak but consistent correlations) which can be leveraged by shallow learning methods to improve predictions of diameter at breast height, and aboveground biomass. This finding suggests that the information retrieved from the local context serves as a proxy for underlying ecological mechanisms that exert influence on the individual tree diameter and therefore aboveground biomass, as a result of local adaptations to microclimate, edaphic conditions and biotic factors. We conclude that the use of UAV LiDAR surveys and the integration of the spatial associations of tree heights is an efficient approach to incorporate context and thus enhance forest biomass surveying.

Supporting Information

| Annex I: Context Detection

The distance range selected around each tree to compute neighborhood metrics (i.e. context detection), was conducted based on the peak of significance (determined using the standard z-score) of local spatial autocorrelation (using Local Moran's I_i) as function of increasing distance, in steps of 10 m.

Local Moran's I_i is a spatial statistic that relates attribute similarity to locational similarity, mapping the autocorrelation of individual tree heights across the geographical space, as defined above (Eq. 1, in Section 3.1). The expression below (Eq. 6) defines the z-score, which is used to measure the significance of tree-height clustering. Z-scores shows the significance of the clustering by subtracting the observed I_i values from the expectation (i.e. $E[I_i]$), and normalizing over the standard deviation of I_i. This produces a distance metric in units of standard deviations. $E[I_i]$ is the expected value of local Moran's I_i under the null hypothesis of no spatial autocorrelation.

$$z_{score} = \frac{I_i - E[I_i]}{\sqrt{V[I_i]}}, \tag{6}$$

Neighborhood size was determined according to the significance of spatial autocorrelation (defined as local Moran's I_i) as function of distance, via the standard z-score. The expected value of Moran's I under the null hypothesis of no spatial autocorrelation is:

$$E[I_i] = -\frac{\sum_{j=1}^{m} w_{i,j}}{m-1} = -\frac{1}{m-1} \tag{7}$$

where m equals the total number of trees in the neighborhood. At large sample sizes (i.e. for increasing values of m), the expected value approaches zero. The spatial weights allocated to each neighboring tree j are standardized [68], such that for each tree i, $\sum_j w_{i,j} = 1$. Finally, the variance of local Moran's I_i is defined as the expectation of the square of I_i, minus the square of the expectations of I_i:

$$V[I_i] = E[I^2] - E[I_i]^2 \tag{8}$$

| Annex II: Preprocessing Tasks

To guarantee that only the trees detected by LiDAR were included in the regression analysis, a pre-processing step was necessary (marked * in Figure 3). First, understory trees that passed unnoticed to the UAV LiDAR survey were removed. Second, we filtered clumped trees by selecting the field-based measurement of the highest tree when two ground measurements were less than 1 m apart, while removing the measurement of the shorter tree. Third, we corrected for a crown shift effect, i.e. some high and skewed trees were affected by the presence of a smaller neighboring tree (affecting less than 5% of the trees) being closer to its corresponding individual tree crown polygon centroid, thus introducing a wrongly allocated label between the field-based measurement and the LiDAR-derived metrics. The resulting distribution is shown in Figure 14b.

A second data preparation step was executed prior to the morphometric analysis of tree assemblages. (marked ** in Figure 3). First, single tree crown polygons were merged based on either local Moran's I_i [60] or SL_i [64] (Section 2.3). These new larger polygons describe the two-dimensional projection of tree assemblages. Then, as our interest focused on the extent and shape of the tree assemblages, the inner borders of the merged polygons were discarded. To reduce computation time, the polygon shapes were simplified by reducing the number of vertices and edges to 70% while keeping the polygon shape.

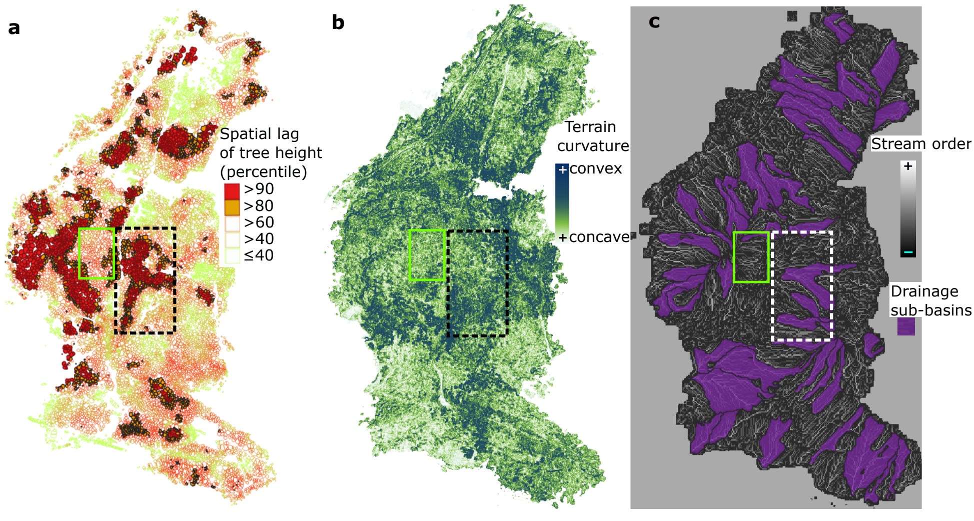

FIGURE 10 **a**: Spatial lag of tree height derived from the individual tree crown polygon dataset. **b**: Map of terrain curvature derived from LiDAR ground-returns. **c**: Hydrological network (Strahler's stream order) [114]. In all three panels, the dashed box indicates an area favored by surface hydrological conditions, hosting an assemblage of trees in the >90 % percentile of spatial lag of tree height. The solid green box indicates an area at a hilltop, unfavored by surface hydrological processes, more exposed to windstorm disturbance, and hosting an assemblage of trees in the < 60% percentile of spatial lag of tree height.

| Annex III: Morphometry of Tree Assemblages

In the coniferous forest site considered in this study, the spatial distribution of SL_i of tree heights presents directional anisotropy, stretching across preferential areas which seem to match sheltered sectors of the forest, such as concave thalwegs. Figure 10 highlights two neighboring areas with contrasting values of SL_i, which may indicate that surface hydrology processes and terrain exposure (i.e. terrain convexity) condition tree growth at the group level. No management activities or harvesting have occurred in the study area, apart from a 2005 clearing event that partially affected SP-6. Consequently, the forest structure can be considered shaped primarily by natural abiotic and biotic factors.

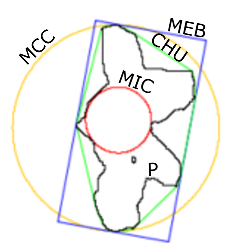

FIGURE 11 Calculation of elementary geometries fitted to an exemplary tree assemblage. P: polygon of tree assemblage (black line). MCC: minimum circumscribed cirle (in green). MIC: maximum inscribed circle (in red). CHU: convex hull (in yellow). MEB: minimum enclosing box containing P (in blue).

The morphometric analysis was conducted by taking into account the outer borders of tree assemblages defined either by SL_i, or by local Moran's I_i (delineated as explained in Section 2.3; results shownin Figure 5). The 20 basic morphometric variables (Table 3) result from fitting elementary geometries to the tree assemblage polygon. The 20 derived variables (Table 4) are adimensional parameters (except for concavity, in m^2) obtained by combining the basic parameters.

TABLE 3 Twenty basic morphometric variables derived from the tree assemblage polygon dataset (as described in Güler et al., 2021) [73]. P: polygon of a tree assemblage.

Basic parameters	Description	units
XPOL	Easting of P centroid	m
YPOL	Northing of P centroid	m
APOL	Area of P	m^2
PPOL	Perimeter of P	m
LPOL	Major axis' length of P	m
WPOL	Minor axis' length of P	m
N-S	North-South alignment of P, defined as $\lvert sin(azimuth)\rvert$ of major axis	$\varnothing$
ABOB	Area of the bounding box fully containing P	m^2
PBOB	Perimeter of the bounding box fully containing P	m
AMEB	Area of minimum enclosing box	m^2
PMEB	Perimeter of minimum enclosing box	m
ACHU	Area of the convex hull fully containing P	m^2
PCHU	Perimeter of the convex hull fully containing P	m
AMCC	Area of the minimum circumscribed circle enclosing P	m^2
PMCC	Perimeter of the minimum circumscribed circle enclosing P	m
RMCC	Radius of the minimum circumscribed circle enclosing P	m
AMIC	Area of the maximum inscribed circle enclosing P	m^2
PMIC	Perimeter of the maximum inscribed circle enclosing P	m
RMIC	Radius of the maximum inscribed circle enclosing P	m

In Figure 12 we show the morphometric variables, obtained from the delineated tree assemblages, that showed the highest correlation with spatial lag of tree heights.

TABLE 4 20 morphometric variables derived from the tree assemblage polygon dataset (as described in [73]). P: tree assemblage polygon. A: area of P. L: length of major axis of P. W: width of minor axis of P (i.e. width). ACHU: area of convex hull fully containing P. RMCC: radius of minimum circumscribed circle. PCHU: perimeter of convex hull fully containing P. AMEB: area of minimum enclosing box.

Derived parameters	Name	Definition	Source
LTWR	Length-to-width ratio	L/W	[87]
WTLR	Width-to-Length ratio	W/L	[88]
ELLF	Ellipticity Factor	$\lvert L-W\rvert/(L+W)$	[89]
CIRR	Circularity Ratio	P^2/A	[90]
ZFOR	Zăvoianu's Form Factor	$(16A)/P^2$	[91]
COMF	Compactness Factor	$P/(4\pi A)^{0.5}$	[73]
MCIR	Miller's Circularity Ratio	$(4\pi A)/P^2$	[92]
DISM	Dispersion Measure	$1-[(4\pi A)^{0.5}/P]$	[90]
COMI	Complexity Index	$1-[(4\pi A)/P^2]$	[73]
HFOR	Horton's Form Factor	A/L^2	[87]
ELOF	Elongation Factor	$(4A/\pi)^{0.5}/L$	[93]
LEMR	Lemniscate Ratio	$(\pi L^2)/4A$	[94]
REGF	Regularity Factor	$(\pi LW)/4A$	[89]
SHAF	Shape Factor	$[(4\pi A)/P^2]\times(L/W)$	[89]
CONV	Convexity	$PCHU/P$	[95]
CONC	Concavity	$ACHU-A$	[72]
SOLI	Solidity	$A/ACHU$	[96]
RECT	Rectangularity	$A/AMEB$	[97]
ROUN	Roundness	$(4\pi A)/(PCHU)^2$	[95]
SPHE	Sphericity	$(4A/\pi)^{0.5}/(2\times RMCC)$	[98]

669

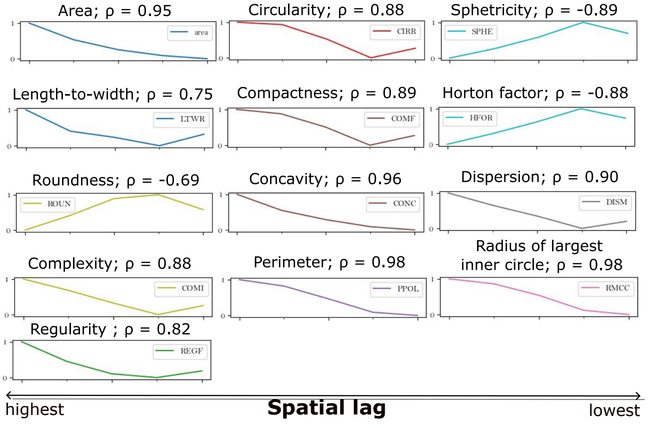

FIGURE 12 Correlation coefficients between (i) the most prominent morphometric variables derived from tree assemblages and (ii) spatial lag. The five ticks on the x-axis correspond to assemblage groups ordered from high to low spatial lag (left to right).

Annex IV: Training, Validation and Test of results

Nested cross-validation (NCV) [83] follows the updated and established recommendations to achieve an unbiased estimate of the generalization error, while making optimal use of the limited available data. It is an evaluation method for determining the accuracy of point estimates and confidence intervals for prediction errors. As a modification developed from standard cross-validation [115], NCV improves estimates of prediction accuracy and confidence intervals by accounting for the correlation between error estimates in different folds, an inconvenient phenomenon affecting standard cross-validation that may render error estimates overly optimistic. How NCV is implemented is shown in Figure 13. The entire algorithmic routine of NCV is presented immediately below. The input data (i.e. *X*,*Y*) corresponds to the set of predictors (i.e. *X*), and the target variable DBH (i.e. *Y*), respectively.

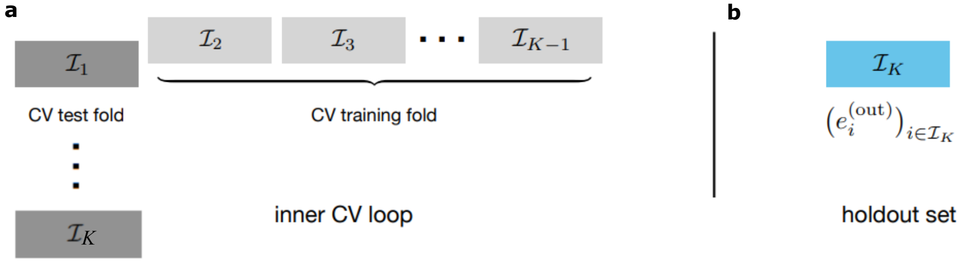

FIGURE 13 Visualization of 10-fold nested cross-validation (CV). **a**: at each of the K steps ($K = 10$), we perform standard cross-validation for model training (light grey folds), holding one of the folds out of the inner CV loop (dark grey fold). **b**: The fresh holdout folds (in blue) are never used for hyperparameter optimization or feature selection (figure adapted from Bates et al., 2021 [83]).

Algorithm 1: Nested cross-validation

Input: data (X, Y), fitting algorithm A, loss ℓ, number of folds K, number of repetitions R

procedure Nested cross-validation *(X,Y)* `// ▷ primary algorithm;`

$es \leftarrow [\,]$ `// ▷ initialize empty vectors;`

$a\_list \leftarrow [\,]$ `// ▷ (a) terms;`

$b\_list \leftarrow [\,]$ `// ▷ (b) terms;`

for $r \in \{1, ..., R\}$ **do**

Randomly assign points to folds $I_1, \ldots, I_K$;

for $k \in \{1, ..., K\}$ **do**

`// ▷ outer CV loop ;`

$e^{(\text{in})} \leftarrow$ inner cross-validation$(X, Y, \{I_1, \ldots, I_K\} \setminus I_k)$ `// ▷ inner CV loop ;`

$\hat{\theta} \leftarrow A((X_i, Y_i)_{i \in I \setminus I_k})$;

$e^{(\text{out})} \leftarrow (\ell(\hat{f}(X_i, \hat{\theta}), Y_i))_{i \in I_k}$;

$a\_list \leftarrow$ append$(a_list, (mean(e^{(in)}) - mean(e^{(out)}))^2)$;

$b\_list \leftarrow$ append$(b_list, var(e^{(out)})/|I_k|)$;

$es \leftarrow$ append(es, $e^{(\text{in})}$)

$\widehat{MSE} \leftarrow mean(a\_list) - mean(b\_list)$;

$\widehat{Err}^{(NCV)} \leftarrow mean(es)$;

return:$(\widehat{Err}^{(NCV)}, \widehat{MSE})$ `// ▷ prediction error estimate and MSE estimate ;`

procedure Inner cross-validation (X, Y, $\{I_1, ..., I_{K-1}\}$) `// ▷ inner cross-validation subroutine ;`

$e^{(in)} \leftarrow [\,]$;

for $k \in \{1, ..., K-1\}$ **do**

$\hat{\theta} \leftarrow A((X_i, Y_i)_{i \in I_i \cup \ldots \cup I_{K-1} \setminus I_k})$;

$e^{(temp)} \leftarrow (\ell(\hat{f}(X_i, \hat{\theta})), Y_i))_{i \in I_k}$;

$e^{(in)} \leftarrow append(e^{(in)}, e^{(temp)})$;

return: $e^{(in)}$;

Output: Nested cross-validation *(X,Y)*

Annex V: Distribution Shift Between CP-trees and SP-trees

Here below, we show the joint distributions of DBH and tree height in the two datasets considered (SP-trees, CP-trees) in order to highlight how differently distributed they are—both in field-based inventory (Figure 14a) and in the dataset captured by the UAV LiDAR system (Figure 14b). The joint distributions of DBH and tree height in both CP and SP-datasets show a shift between the two [116], which justifies treating them separately. The kernel probability distribution of heights shows that the SP-dataset contains a higher amount of short trees (i.e. 3-10 m), which cover a wide range of DBH values (i.e. 5-20 cm). Also, the range of DBH is broader in the SP-dataset compared to the CP-dataset, and the SP-instances do not exhibit an accumulation in the center as evident as the one observed in the CP-dataset.

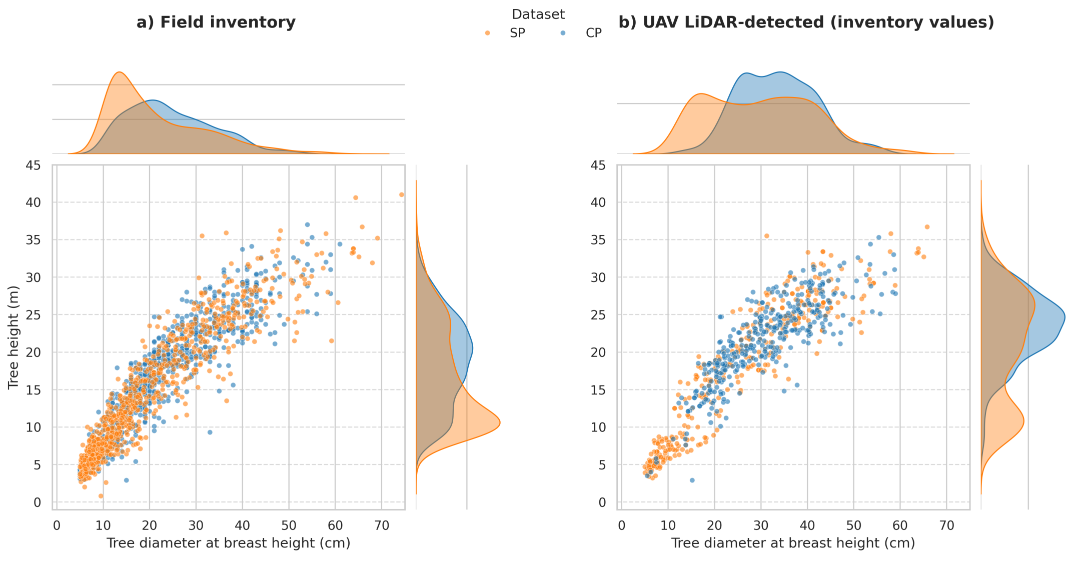

FIGURE 14 Joint distributions of diameter at breast-height and tree height from field-based inventory data. a: Field inventory; b: trees in field inventory detected by the UAV LiDAR system. It should be noted that the two datasets (i.e. SP-trees, CP-trees) are differently distributed—i.e. there is a shift [116] between Sparse Measurement Plots (SP) and Continuous Measurement Plots (CP) datasets.

Annex VI: Elevation Map of the Study Site and Location of SP-plots

We provide the digital elevation model of the study area (Figure 15, a) to understand differences in flight heights (Figure 2) and to complement the information given on terrain exposure and surface hydrology (Figure 10). Figure 15, (b) shows the five rejected SP-plots and one valid (i.e. SP-18), for comparison. Among the rejected SP-plots, 1, 2, 9 and 10 show an insufficiently descriptive CHM, while SP-14 shows an intractable allocation of ground-based labels. All five rejected SP-plots were discarded before starting the modelling process, so they did not take part in the regression experiments.

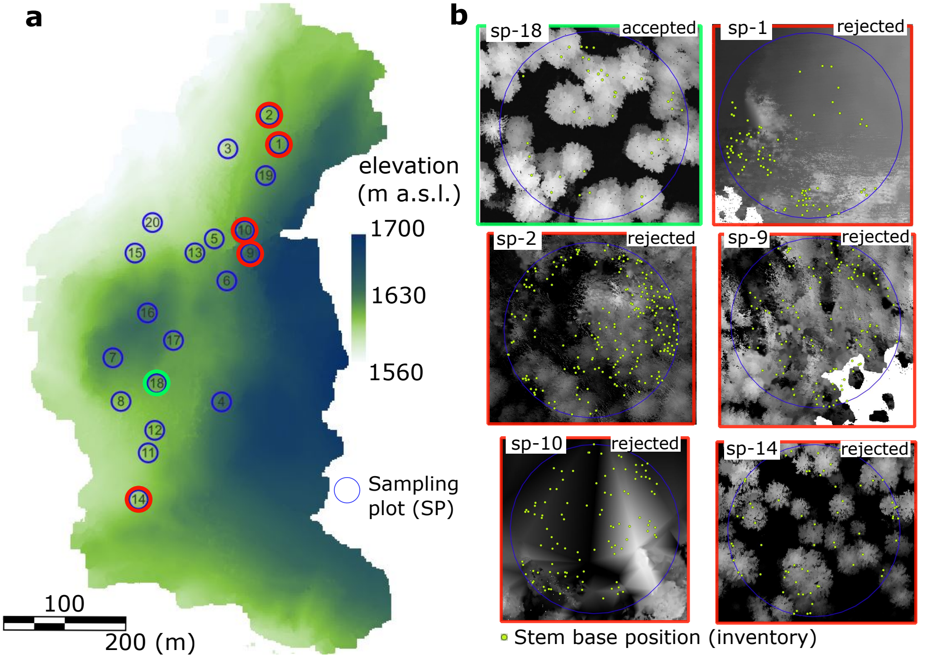

FIGURE 15 **a:** Digital elevation model of the study area. a.s.l.: elevation above sea level, in m. The blue circles represent the SP-plots, numbered by their ID code (1-20). The green and red circles refer to the plots shown in panel b. **b:** Five SP-plots rejected and one valid (SP-18) given for comparison of contrasting quality of canopy height models, derived from the UAV LiDAR point cloud data. In all six SP-plots, the yellow dots indicate the location of tree stems according to the field-based inventory.

Annex VII: Importance of predictors considered

Figure 16 shows the importance of all predictors initially considered (41) in the context-aware regression experiment. Results show the permutation importances for the best performing model (i.e. AdaBoost) in both datasets (CP-dataset and SP-dataset).

Besides tree-level and context-based predictors, we included topographic wetness index (TWI) as a predictor, which is a well-established environmental factor determining favorable hydrological conditions for tree growth. TWI is a steady state wetness index used to evaluate topography-dependent surface hydrology processes. According to the established definition [69], TWI is calculated as $\frac{a}{tan(b)}$, where a represents the upslope area draining through the point of interest, and b indicates the local slope. The parameterization considered to calculate TWI followed the suggestions of Kopecký et al. (2021) [117] for soil moisture estimation. In order to discern how much the contribution of TWI is influenced by granularity, we calculated it at a 2 m, 5 m and 10 m resolution, and included it as separate predictors.

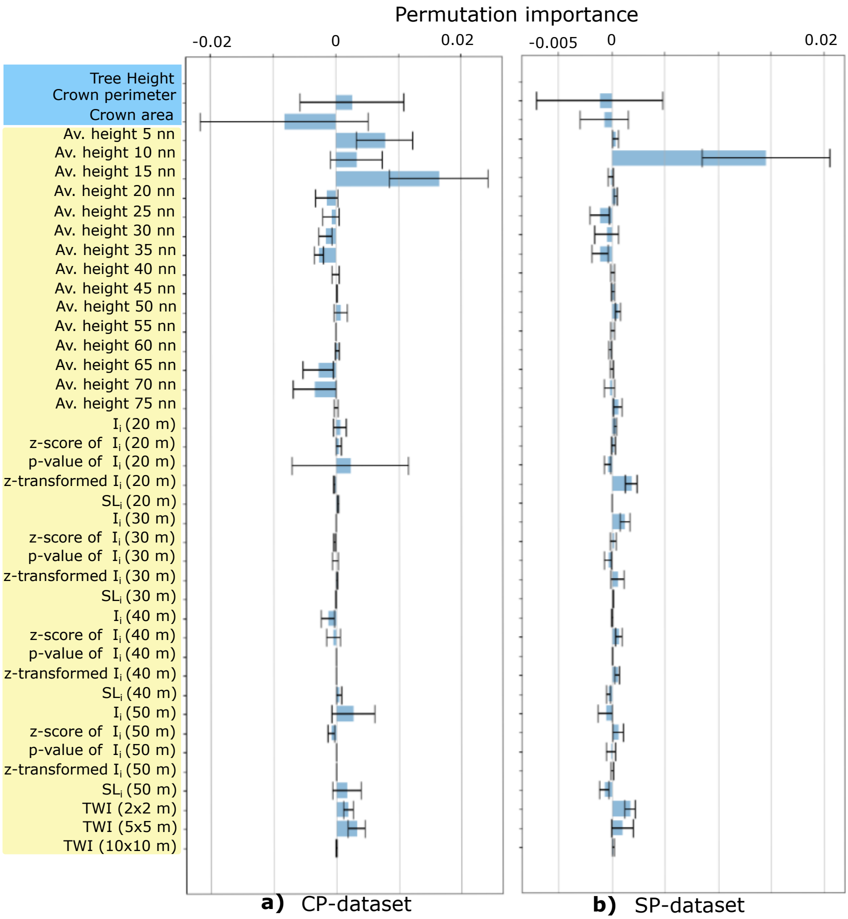

FIGURE 16 Inspection of predictors' importance via the permutation method [84] in the AdaBoost regression experiment in context-aware conditions. The left panel **(a)** shows results in the Continuous Measurement Plot (CP) dataset, and the right panel **(b)** shows results in the Sparse Measurement Plot (SP) dataset. Bar length and error bar show the mean and standard deviation of a predictor's importance, respectively. A negative mean value indicates that a predictor is less useful than when being randomly shuffled, so it lowers the model's predictive performance. Predictors highlighted in blue are individual tree traits; predictors highlighted in yellow are context-based (i.e. either neighborhood metrics or topographic wetness index, TWI). In both datasets, it can be noted how the average heights of the nearest 5-15 neighbors (nn) stand out as the strongest predictors, outperforming crown perimeter and crown area. In both plots (**a** and **b**), individual tree height (with importance: 0.85 in CP-dataset; 1.3 in SP-dataset) has been removed to facilitate visual comparison of the remaining predictors.

709

Graphical Abstract

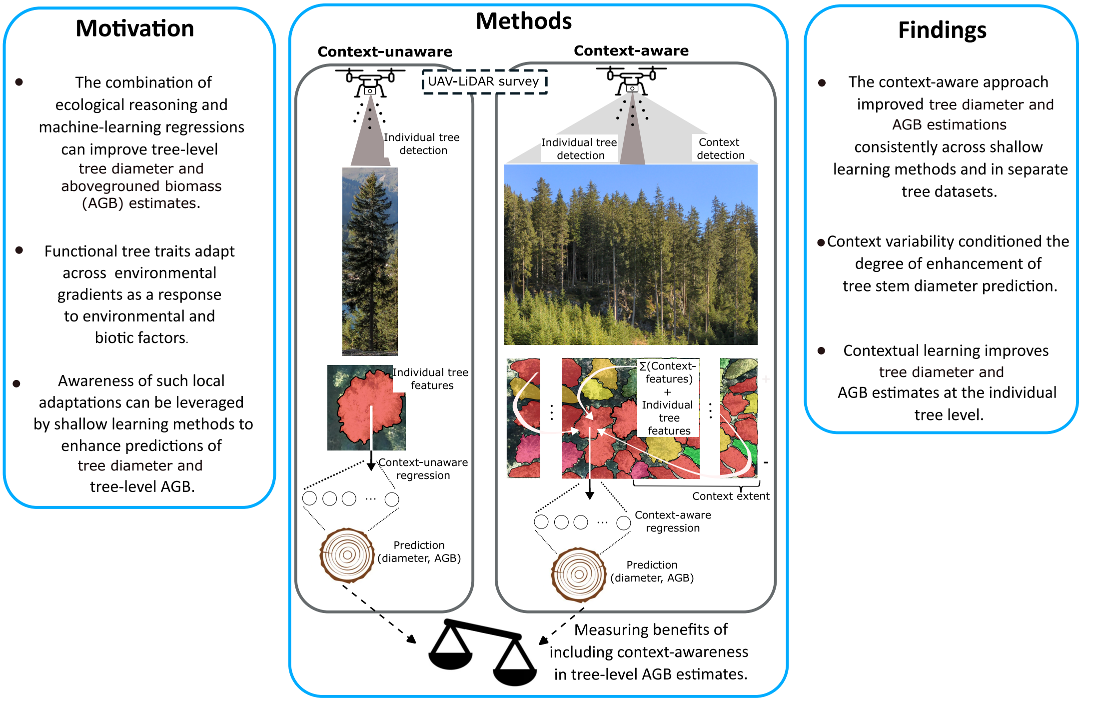

FIGURE 17 Graphical Abstract of the study.

References

[1] Fatichi S, Pappas C, Zscheischler J, Leuzinger S. Modelling carbon sources and sinks in terrestrial vegetation. New Phytologist 2019;221(2):652–668.

[2] Pörtner HO, Roberts DC, Adams H, Adler C, Aldunce P, Ali E, et al. Climate change 2022: Impacts, adaptation and vulnerability. IPCC Geneva, Switzerland; 2022.

[3] Friedlingstein P, Jones MW, O'sullivan M, Andrew RM, Hauck J, Peters GP, et al. Global carbon budget 2019. Earth System Science Data 2019;11(4):1783–1838.

[4] Baccini A, Walker W, Carvalho L, Farina M, Sulla-Menashe D, Houghton R. Tropical forests are a net carbon source based on aboveground measurements of gain and loss. Science 2017;358(6360):230–234.

[5] Gundersen P, Thybring EE, Nord-Larsen T, Vesterdal L, Nadelhoffer KJ, Johannsen VK. Old-growth forest carbon sinks overestimated. Nature 2021;591(7851):E21–E23.

[6] Duncanson L, Armston J, Disney M, Avitabile V, Barbier N, Calders K, et al. The importance of consistent global forest aboveground biomass product validation. Surveys in geophysics 2019;40:979–999.

[7] Santini F, Kefauver SC, Resco de Dios V, Araus JL, Voltas J. Using unmanned aerial vehicle-based multispectral, RGB and thermal imagery for phenotyping of forest genetic trials: A case study in Pinus halepensis. Annals of Applied Biology 2019;174(2):262–276.

[8] Yao W, Krull J, Krzystek P, Heurich M. Sensitivity analysis of 3D individual tree detection from LiDAR point clouds of temperate forests. Forests 2014;5(6):1122–1142.

[9] Dalponte M, Coomes DA. Tree-centric mapping of forest carbon density from airborne laser scanning and hyperspectral data. Methods in ecology and evolution 2016;7(10):1236–1245.

[10] Kükenbrink D, Hueni A, Schneider FD, Damm A, Gastellu-Etchegorry JP, Schaepman ME, et al. Mapping the irradiance field of a single tree: Quantifying vegetation-induced adjacency effects. IEEE Transactions on Geoscience and Remote Sensing 2019;57(7):4994–5011.

[11] Cabo C, Ordóñez C, López-Sánchez CA, Armesto J. Automatic dendrometry: Tree detection, tree height and diameter estimation using terrestrial laser scanning. International journal of applied earth observation and geoinformation 2018;69:164–174.

[12] Kukkonen M, Maltamo M, Korhonen L, Packalen P. Multispectral airborne LiDAR data in the prediction of boreal tree species composition. IEEE Transactions on Geoscience and Remote Sensing 2019;57(6):3462–3471.

[13] Bertness MD, Callaway R. Positive interactions in communities. Trends in ecology & evolution 1994;9(5):191–193.

[14] Maestre FT, Callaway RM, Valladares F, Lortie CJ. Refining the stress-gradient hypothesis for competition and facilitation in plant communities. Journal of ecology 2009;97(2):199–205.

[15] Muscarella R, Messier J, Condit R, Hubbell SP, Svenning JC. Effects of biotic interactions on tropical tree performance depend on abiotic conditions. Ecology 2018;99(12):2740–2750.

[16] Valladares F, Niinemets Ü. Shade tolerance, a key plant feature of complex nature and consequences. Annual Review of Ecology, Evolution, and Systematics 2008;39(1):237–257.

[17] Hao Y, Widagdo FRA, Liu X, Quan Y, Dong L, Li F. Individual tree diameter estimation in small-scale forest inventory using UAV laser scanning. Remote Sensing 2020;13(1):24.

[18] Yang Z, Liu Q, Luo P, Ye Q, Sharma RP, Duan G, et al. Nonlinear mixed-effects height to crown base model based on both airborne LiDAR and field datasets for Picea crassifolia Kom trees in northwest China. Forest Ecology and Management 2020;474:118323.

[19] Liu X, Hao Y, Widagdo FRA, Xie L, Dong L, Li F. Predicting height to crown base of Larix olgensis in Northeast China Using UAV-LiDAR data and nonlinear mixed effects models. Remote Sensing 2021;13(9):1834.

[20] Sun S, Cao QV, Cao T. Evaluation of distance-independent competition indices in predicting tree survival and diameter growth. Canadian Journal of Forest Research 2019;49(5):440–446.

[21] Zhang B, Sajjad S, Chen K, Zhou L, Zhang Y, Yong KK, et al. Predicting tree height-diameter relationship from relative competition levels using quantile regression models for Chinese fir (Cunninghamia lanceolata) in Fujian province, China. Forests 2020;11(2):183.

[22] Lo CS, Lin C. Growth-competition-based stem diameter and volume modeling for tree-level forest inventory using airborne LiDAR data. IEEE Transactions on Geoscience and Remote Sensing 2012;51(4):2216–2226.

[23] Potvin C, Dutilleul P. Neighborhood effects and size-asymmetric competition in a tree plantation varying in diversity. Ecology 2009;90(2):321–327.

[24] Ratcliffe S, Holzwarth F, Nadrowski K, Levick S, Wirth C. Tree neighbourhood matters–Tree species composition drives diversity–productivity patterns in a near-natural beech forest. Forest Ecology and Management 2015;335:225–234.

[25] Andersen HE, McGaughey RJ, Reutebuch SE. Estimating forest canopy fuel parameters using LIDAR data. Remote sensing of Environment 2005;94(4):441–449.

[26] Næsset E, Økland T. Estimating tree height and tree crown properties using airborne scanning laser in a boreal nature reserve. Remote Sensing of Environment 2002;79(1):105–115.

[27] Rijal B, Weiskittel AR, Kershaw Jr JA. Development of height to crown base models for thirteen tree species of the North American Acadian Region. The Forestry Chronicle 2012;88(1):60–73.

[28] Antonio N, Tome M, Tome J, Soares P, Fontes L. Effect of tree, stand, and site variables on the allometry of Eucalyptus globulus tree biomass. Canadian Journal of Forest Research 2007;37(5):895–906.

[29] Hyyppä E, Yu X, Kaartinen H, Hakala T, Kukko A, Vastaranta M, et al. Comparison of backpack, handheld, under-canopy UAV, and above-canopy UAV laser scanning for field reference data collection in boreal forests. Remote Sensing 2020;12(20):3327.

[30] Li N, Ho CP, Xue J, Lim LW, Chen G, Fu YH, et al. A Progress Review on Solid-State LiDAR and Nanophotonics-Based LiDAR Sensors. Laser & Photonics Reviews 2022;16(11):2100511.

[31] Oehmcke S, Li L, Revenga JC, Nord-Larsen T, Trepekli K, Gieseke F, et al. Deep learning based 3D point cloud regression for estimating forest biomass. In: Proceedings of the 30th International Conference on Advances in Geographic Information Systems; 2022. p. 1–4.

[32] Réjou-Méchain M, Barbier N, Couteron P, Ploton P, Vincent G, Herold M, et al. Upscaling forest biomass from field to satellite measurements: sources of errors and ways to reduce them. Surveys in Geophysics 2019;40(4):881–911.

[33] Xu D, Wang H, Xu W, Luan Z, Xu X. LiDAR applications to estimate forest biomass at individual tree scale: Opportunities, challenges and future perspectives. Forests 2021;12(5):550.

[34] Biging GS, Dobbertin M. Evaluation of competition indices in individual tree growth models. Forest science 1995;41(2):360–377.

[35] Schiefer F, Kattenborn T, Frick A, Frey J, Schall P, Koch B, et al. Mapping forest tree species in high resolution UAV-based RGB-imagery by means of convolutional neural networks. ISPRS Journal of Photogrammetry and Remote Sensing 2020;170:205–215.

[36] Marques O, Barenholtz E, Charvillat V. Context modeling in computer vision: techniques, implications, and applications. Multimedia Tools and Applications 2011;51:303–339.

[37] Zhao R, Ouyang W, Li H, Wang X. Saliency Detection by Multi-Context Deep Learning. In: Proceedings of the IEEE Conference on Computer Vision and Pattern Recognition (CVPR); 2015. p. 1265–1274.

[38] Chu HJ, Wu CF, Lin YP. Incorporating spatial autocorrelation with neural networks in empirical land-use change models. Environment and Planning B: Planning and Design 2013;40(3):384–404.

[39] Luo W, Li Y, Urtasun R, Zemel R. Understanding the effective receptive field in deep convolutional neural networks. Advances in neural information processing systems 2016;29.

[40] Yang W, Tan RT, Feng J, Liu J, Guo Z, Yan S. Deep joint rain detection and removal from a single image. In: Proceedings of the IEEE conference on computer vision and pattern recognition; 2017. p. 1357–1366.

[41] Liu YF, Jaw DW, Huang SC, Hwang JN. DesnowNet: Context-aware deep network for snow removal. IEEE Transactions on Image Processing 2018;27(6):3064–3073.

[42] Mittal S, Sharma I, Kumar A, et al. Comparative Analysis of Shallow Learning and Deep Learning. In: 2023 International Conference on Next Generation Electronics (NEleX) IEEE; 2023. p. 1–8.

[43] Jafari F, Moradi K, Shafiee Q. Shallow learning vs. deep learning in engineering applications. In: Shallow Learning vs. Deep Learning: A Practical Guide for Machine Learning Solutions Springer; 2024.p. 29–76.

[44] Switzerland I, ICOS-CH Ecosystem Station Davos; 2026. Accessed: 2026-01-19. https://www.icos-switzerland.ch/davos.

[45] Heiskanen J, C B, N B, C C, H C, B G, et al. The Integrated Carbon Observation System in Europe. Bulletin of the American Meteorological Society 2022;103(3):E855–E872.

[46] Burri S, Long-Term Environmental Research–The Davos-Seehornwald Site. ETH Zurich; 2019. https://doi.org/10.3929/ethz-b-000328277.

[47] Swiss FluxNet, Site History: CH-DAV; 2024. https://www.swissfluxnet.ethz.ch/index.php/sites/site-info-ch-dav/history/, accessed: 2026-01-12.

[48] WSL, Long-term Forest Ecosystem Research (LWF); 2023. https://www.wsl.ch/en/about-wsl/organisation/programmes-and-initiatives/, accessed: 2023-02-04.

[49] TreeNet, Biological Drought and Growth Indicator Network; 2023. https://treenet.info/, accessed: 2023-02-04.

[50] Swiss FluxNet, Swiss FluxNet: National Greenhouse Gas Flux Measurement Network; 2023. https://www.swissfluxnet.ethz.ch/, accessed: 2023-02-04.

[51] ICOS, Integrated Carbon Observation System; 2023. https://www.icos-cp.eu/, accessed: 2023-02-04.

[52] ICP Forests, International Co-operative Programme on Assessment and Monitoring of Air Pollution Effects on Forests; 2023. http://icp-forests.net/, accessed: 2023-02-04.

[53] LTER, Integrated European Long-Term Ecosystem, Critical Zone and Socio-ecological Research; 2023. https://elter-ri.eu/, accessed: 2023-02-04.

[54] Revenga JC, Trepekli K, Oehmcke S, Jensen R, Li L, Igel C, et al. Above-Ground Biomass Prediction for Croplands at a Sub-Meter Resolution Using UAV–LiDAR and Machine Learning Methods. Remote Sensing 2022;14(16):3912.

[55] Davidson L, Mills J, Haynes I, Augarde C, Bryan P, Douglas M. Airborne to UAS LiDAR: An analysis of UAS LiDAR ground control targets. ISPRS Geospatial Week 2019;.

[56] Swiss Federal Institute for Forest, Snow and Landscape Research (WSL). Methods of the Sanasilva Inventory. Swiss Federal Institute for Forest, Snow and Landscape Research (WSL); 2023.

[57] Gielen B, Acosta M, Altimir N, Buchmann N, Cescatti A, Ceschia E, et al. Ancillary vegetation measurements at ICOS ecosystem stations. International Agrophysics 2018;32(4):645–664.

[58] ICOS RI. ICOS Handbook 2019. Integrated Carbon Observation System (ICOS) Research Infrastructure; 2019.

[59] Chen Q GP Baldocchi D, M K. Isolating Individual Trees in a Savanna Woodland Using Small Footprint Lidar Data. In: Photogrammetric Engineering and Remote Sensing, 72(8): 923-932; 2006. p. 923–932.

[60] Anselin L. Local indicators of spatial association—LISA. Geographical analysis 1995;27(2):93–115.

[61] Anselin L, Rey SJ. Perspectives on spatial data analysis. In: Perspectives on spatial data analysis Springer; 2010.p. 1–20.

[62] Breunig MM, Kriegel HP, Ng RT, Sander J. LOF: identifying density-based local outliers. In: Proceedings of the 2000 ACM SIGMOD international conference on Management of data; 2000. p. 93–104.

[63] Liu FT, Ting KM, Zhou ZH. Isolation forest. In: 2008 eighth ieee international conference on data mining IEEE; 2008. p. 413–422.

[64] Anselin L, Syabri I, Kho Y. GeoDa: an introduction to spatial data analysis. In: Handbook of applied spatial analysis: Software tools, methods and applications Springer; 2009.p. 73–89.

[65] Cressie N. Statistics for spatial data. John Wiley & Sons; 2015.

[66] Getis A, Ord JK. The analysis of spatial association by use of distance statistics. In: Perspectives on spatial data analysis Springer; 2010.p. 127–145.

[67] Westerholt R, Resch B, Mocnik FB, Hoffmeister D. A statistical test on the local effects of spatially structured variance. International Journal of Geographical Information Science 2018;32(3):571–600.

[68] Anselin L, et al. Spatial econometrics. A companion to theoretical econometrics 2001;310330.

[69] Beven KJ, Kirkby MJ. A physically based, variable contributing area model of basin hydrology/Un modèle à base physique de zone d'appel variable de l'hydrologie du bassin versant. Hydrological sciences journal 1979;24(1):43–69.

[70] Mohamedou C, Tokola T, Eerikäinen K. LiDAR-based TWI and terrain attributes in improving parametric predictor for tree growth in southeast Finland. International journal of applied earth observation and geoinformation 2017;62:183–191.

[71] ESRI. ArcGis Pro: Implementation Guide. Redlands, California; 2021, www.esri.com.

[72] Landini G. Particles8 class: An ImageJ plugin for estimating various statistics of binary 8- connected particles.; 2010.

[73] Güler C, Beyhan B, Tağa H. PolyMorph-2D: An open-source GIS plug-in for morphometric analysis of vector-based 2D polygon features. Geomorphology 2021;386:107755.

[74] Steiniger S, Blake L. OpenJUMP software; 2022.

[75] Freund Y, Schapire RE. A decision-theoretic generalization of on-line learning and an application to boosting. Journal of computer and system sciences 1997;55(1):119–139.

[76] Friedman JH. Greedy function approximation: a gradient boosting machine. Annals of statistics 2001;p. 1189–1232.

[77] Schapire RE. Explaining adaboost. Empirical Inference: Festschrift in Honor of Vladimir N Vapnik 2013;p. 37–52.

[78] Tibshirani R. Regression shrinkage and selection via the lasso. Journal of the Royal Statistical Society: Series B (Methodological) 1996;58(1):267–288.

[79] Ho TK. Random decision forests. In: Proceedings of 3rd international conference on document analysis and recognition, vol. 1 IEEE; 1995. p. 278–282.

[80] Vidaurre D, Bielza C, Larranaga P. A survey of L1 regression. International Statistical Review 2013;81(3):361–387.

[81] Gryc V, Horáček P. Variability in density of spruce (Picea abies [L.] Karst.) wood with the presence of reaction wood. Journal of forest science 2007;53(3):129–137.

[82] Scrinzi G, Galvagni D, Marzullo L. I nuovi modelli dendrometrici per la stima delle masse assestamentali in Provincia di Trento. Provincia autonoma di Trento. Servizio foreste e fauna; 2010.

[83] Bates S, Hastie T, Tibshirani R. Cross-validation: what does it estimate and how well does it do it? arXiv preprint arXiv:210400673 2021;.

[84] Altmann A, Toloşi L, Sander O, Lengauer T. Permutation importance: a corrected feature importance measure. Bioinformatics 2010;26(10):1340–1347.

[85] Wilcoxon F. Individual comparisons by ranking methods. Springer; 1992.

[86] Cliff N. Dominance statistics: Ordinal analyses to answer ordinal questions. Psychological bulletin 1993;114(3):494.

[87] Horton RE. Drainage-basin characteristics. Transactions, American geophysical union 1932;13(1):350–361.

[88] Zingg T. Beitrag zur schotteranalyse. PhD thesis, ETH Zurich; 1935.

[89] Buendıa P, Soler C, Paolicchi F, Gago G, Urquieta B, Pérez-Sánchez F, et al. Morphometric characterization and classification of alpaca sperm heads using the Sperm-Class Analyzer® computer-assisted system. Theriogenology 2002;57(4):1207–1218.

[90] Attneave F, Arnoult MD. The quantitative study of shape and pattern perception. Psychological bulletin 1956;53(6):452.

[91] Zăvoianu I. Morfometria bazinelor hidrografice. Editura Academiei Republicii Socialiste România; 1978.

[92] Miller VC. A quantitative geomorphic study of drainage basin characteristics in the clinch mountain area of Virginia and Tennessee, USA. Columbia Univ New York; 1953.

[93] Schumm SA. Evolution of drainage systems and slopes in badlands at Perth Amboy, New Jersey. Geological society of America bulletin 1956;67(5):597–646.

[94] Chorley RJ, Malm E Donald E, Pogorzelski HA. A new standard for estmating drainage basin shape. American Journal of Science 1957;255:138–141.

[95] Horgan GW, Glasbey CA. Uses of digital image analysis in electrophoresis. Electrophoresis 1995;16(1):298–305.

[96] Zunic J, Rosin PL. A new convexity measure for polygons. IEEE Transactions on Pattern Analysis and Machine Intelligence 2004;26(7):923–934.

[97] Rosin PL. Measuring rectangularity. Machine Vision and Applications 1999;11:191–196.

[98] Wadell H. Volume, shape, and roundness of quartz particles. The Journal of Geology 1935;43(3):250–280.

[99] Pillar VD, Duarte LdS, Sosinski EE, Joner F. Discriminating trait-convergence and trait-divergence assembly patterns in ecological community gradients. Journal of Vegetation Science 2009;20(2):334–348.

[100] Goebes P, Schmidt K, Seitz S, Both S, Bruelheide H, Erfmeier A, et al. The strength of soil-plant interactions under forest is related to a Critical Soil Depth. Scientific Reports 2019;9(1):8635.

[101] Green JK, Keenan TF. The limits of forest carbon sequestration. Science 2022;376(6594):692–693.

[102] Valladares F, Gianoli E, Gómez JM. Ecological limits to plant phenotypic plasticity. New phytologist 2007;176(4):749–763.

[103] Valladares F, Arrieta S, Aranda I, Lorenzo D, Sánchez-Gómez D, Tena D, et al. Shade tolerance, photoinhibition sensitivity and phenotypic plasticity of Ilex aquifolium in continental Mediterranean sites. Tree physiology 2005;25(8):1041–1052.

[104] Kraft NJ, Adler PB, Godoy O, James EC, Fuller S, Levine JM. Community assembly, coexistence and the environmental filtering metaphor. Functional ecology 2015;29(5):592–599.

[105] Valladares F, Dobarro I, Sánchez-Gomez D, Pearcy RW. Photoinhibition and drought in Mediterranean woody saplings: scaling effects and interactions in sun and shade phenotypes. Journal of Experimental Botany 2005;56(411):483–494.

[106] Da Silva BC, Basso EW, Bazzan AL, Engel PM. Dealing with non-stationary environments using context detection. In: Proceedings of the 23rd international conference on Machine learning; 2006. p. 217–224.

[107] Naesset E. Determination of mean tree height of forest stands using airborne laser scanner data. ISPRS Journal of Photogrammetry and Remote sensing 1997;52(2):49–56.

[108] Lim KS, Treitz PM. Estimation of above ground forest biomass from airborne discrete return laser scanner data using canopy-based quantile estimators. Scandinavian Journal of Forest Research 2004;19(6):558–570.

[109] Kearsley E, Moonen PC, Hufkens K, Doetterl S, Lisingo J, Boyemba Bosela F, et al. Model performance of tree height-diameter relationships in the central Congo Basin. Annals of Forest Science 2017;74(1):7.

[110] Guillén-Escribà C, Schneider FD, Schmid B, Tedder A, Morsdorf F, Furrer R, et al. Remotely sensed between-individual functional trait variation in a temperate forest. Ecology and Evolution 2021;11(16):10834–10867.

[111] Zheng Z, Zeng Y, Schuman MC, Jiang H, Schmid B, Schaepman ME, et al. Individual tree-based vs pixel-based approaches to mapping forest functional traits and diversity by remote sensing. International Journal of Applied Earth Observation and Geoinformation 2022;114:103074.

[112] Ma X, Migliavacca M, Wirth C, Bohn FJ, Huth A, Richter R, et al. Monitoring plant functional diversity using the reflectance and echo from space. Remote Sensing 2020;12(8):1248.

[113] Wang CJ, Zhang ZX, Wan JZ. Vulnerability of global forest ecoregions to future climate change. Global Ecology and Conservation 2019;20:e00760.

[114] Strahler AN. Hypsometric (area-altitude) analysis of erosional topography. Geological society of America bulletin 1952;63(11):1117–1142.

[115] Berrar D. Cross-Validation. Encyclopedia of Bioinformatics and Computational Biology 2018;1:542–545.

[116] Quionero-Candela J, Sugiyama M, Schwaighofer A, Lawrence ND. Data Set Shift in Machine Learning. MIT Press, Cambridge, Massachusetts; 2009. http://www.acad.bg/ebook/ml/The.MIT.Press.Dataset.Shift.in.Machine.Learning.Feb.2009.eBook-DDU.pdf.

[117] Kopeckỳ M, Macek M, Wild J. Topographic Wetness Index calculation guidelines based on measured soil moisture and plant species composition. Science of the Total Environment 2021;757:143785.